

Level attraction from interference in a two-tone-driven cavity magnonics system


Alan Gardin^{1,2,*}, Guillaume Bourcin², Christian Person², Christophe Fumeaux³,
Romain Lebrun⁴, Isabella Boventer⁴, Giuseppe C. Tettamanzi¹, and Vincent Castel²

¹*Quantum and Nano Technology Group, School of Chemical Engineering, The University of Adelaide, Adelaide, SA 5005, Australia*

²*IMT Atlantique, Lab-STICC, UMR CNRS 6285, 29238 Brest, France*

³*School of Electrical Engineering and Computer Science, The University of Queensland, Brisbane, QLD 4072, Australia*

⁴*Unité Mixte de Physique, CNRS, Thales, Université Paris-Saclay, 91767 Palaiseau, France*

 (Received 10 May 2024; revised 16 September 2024; accepted 17 December 2024; published 23 January 2025)

Coherent and dissipative couplings, respectively characterized by energy level repulsion and attraction, each have different applications for quantum information processing. Thus, a system in which both coherent and dissipative couplings are tunable on demand and *in situ* is tantalizing. A first step towards this goal is the two-tone driving of two bosonic modes, whose experimental signature was shown to exhibit controllable level repulsion and attraction by changing the phase and amplitude of one drive. However, whether the underlying physics is that of coherent and dissipative couplings has not been clarified, and cannot be concluded solely from the measured resonances (or antiresonances) of the system. Here, we show how the physics at play can be analyzed theoretically. Combining this theory with realistic finite-element simulations, we deduce that the observation of level attraction originates from interferences due to the measurement setup, and not dissipative coupling. Beyond the clarification of the origin of level attraction attributed to interference, our work demonstrates how effective Hamiltonians should be derived to appropriately describe the physics.

DOI: [10.1103/PhysRevApplied.23.014048](https://doi.org/10.1103/PhysRevApplied.23.014048)

I. INTRODUCTION

The coherent coupling between two systems corresponds to the coherent exchange of energy between them, and is characterized by energy level repulsion (also known as normal-mode splitting or as anticrossing). This phenomenon is ubiquitous in physics, spanning from the classical coupling of two harmonic oscillators [1] to the coupling of bosonic quasiparticles with two-level systems [2] or other bosonic modes [3]. With respect to quantum information processing, coherent coupling allows quantum information to be converted between light and solid-state degrees of freedom, and is therefore an elementary building block of quantum communication [4–6]. On the other hand, dissipative coupling [7–9], characterized by energy level attraction instead, arises due to the indirect coupling of two modes mediated by a common reservoir [10–12] (e.g., a strongly dissipative auxiliary mode [13], a photonic environment [14–16], metallic leads [17]). The merging of energy levels characterizing dissipative couplings leads to exceptional points [18–21], which can be useful for topological energy transfer [22], and

improved sensitivity for quantum metrology and quantum sensing applications [23,24]. Furthermore, balancing coherent and dissipative couplings, using dissipation engineering and synthetic gauge fields for instance, allows the breaking of time-reversal symmetry and thus the creation of nonreciprocal devices [10–12,25–28]. Therefore, building a system in which both coherent and dissipative couplings coexist and are tunable would be useful to access all the aforementioned applications on a unique versatile platform. However, while both coherent and dissipative couplings can coexist in a single platform, their tunability is usually not practical. For instance, in cavity magnonics implementations [14,15], this requires mechanical rotation of the cavity or of a static magnetic field.

In a system with both coherent and dissipative couplings, the energy spectrum should exhibit both level repulsion and attraction, respectively. A two-tone driving scheme proposed by Grigoryan *et al.* [29] suggested theoretically that such an energy spectrum could be obtained by simultaneously driving two coherently coupled bosonic modes. In a subsequent work, the same authors predicted a tunable cavity-mediated dissipative coupling taking advantage of the same principle [30]. Furthermore, two experiments by Boventer *et al.* [31,32] implemented

*Contact author: alan.gardin@adelaide.edu.au

the original proposal [29], and confirmed tunable level repulsion and attraction in the reflection spectrum.

These results were promising, since it is usually expected that the response of a system to excitations at frequencies close to their normal modes leads to resonances (or antiresonances), with various possible line shapes informing on the underlying physics [33,34]. Notably, in these experiments [31,32], control is performed through the phase and amplitude of a microwave drive, which is better for integration, for instance compared to the vector magnet required in [14,15]. However, inspection of the experimental signature alone is not sufficient because it may not be related to the energy levels. For instance, while dissipative coupling implies level attraction in a variety of platforms such as optomechanics [35], Aharonov-Bohm interferometers [17] or semiconductor microcavities [16], alternative physics can also lead to level attraction, as exemplified in optomechanics [36] or spinor condensates [37]. Furthermore, the model used in the original proposal [29] was phenomenological, and as such it only reproduces the experimental observable, but cannot be used to conclude on the underlying physics. Thus, the physics at play in two-tone driving remains unclear.

In this work, we model a two-tone driving experiment similar to those of [31,32]. Our starting point is the closed-system Hamiltonian of two coherently coupled bosonic modes, whose spectrum is that of level repulsion. To model the two-tone driving and the experimentally accessible quantities, we use quantum Langevin equations (QLEs) and the input-output formalism [38] (Sec. II). This theoretical treatment allows to find an analytical expression for the experimental signature, where both level repulsion and attraction can occur, in contrast with the sole level repulsion expected from the closed-system Hamiltonian. In Sec. III, we use the analytical expressions of Sec. II to understand the origin of the tunable level repulsion and attraction. These insights guide our finite-element simulations of a realistic setup, and allow us to confirm that level attraction can be attributed to an antiresonance due to the destructive interference between the reflection and transmission coefficients. While this explains the level attraction, it does not completely eliminate the possibility of dissipative coupling. To clarify the physics in the presence of the drives, we derive the open-system effective Hamiltonian of the two-tone driven system, and show that the physics remains exclusively that of coherent coupling, despite the observation of level attraction. We conclude in Sec. V.

II. THEORETICAL MODEL AND EXPERIMENTAL OBSERVABLES

A. Quantum Langevin equations

We consider the experimental setup of Fig. 1, where a ferromagnetic sphere made of yttrium-iron-garnet (YIG)

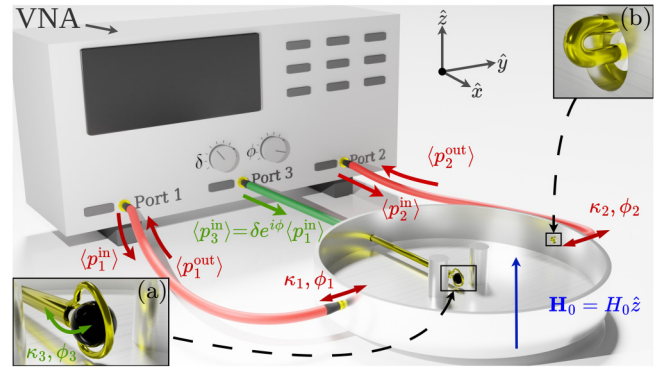


FIG. 1. Schematic of a two-tone driving experiment using a two-post reentrant cavity [39] loaded with a ferromagnetic sphere made of yttrium-iron-garnet (YIG). Ports 1 and 3 are always active and drive respectively the cavity and magnon modes. The cavity is connected to a vector network analyzer (VNA) to measure the reflection at port 1 and the transmission through port 2. Inset (a): the YIG sphere is placed at the center of a loop made by soldering the inner and outer conductor of a coaxial cable, itself placed between the two posts where the cavity mode's magnetic field is strongest. In the picture, the loop is in the x - z plane, and the YIG sphere is biased along \hat{z} by the static magnetic field \mathbf{H}_0 . Inset (b): antenna used to excite the cavity modes.

is placed inside a microwave cavity. The second quantized Hamiltonian of the system enclosed inside the cavity is that of the lowest-order magnon mode (quantized spin wave) coupled to a single cavity mode, described by [9]

$$H_{\text{sys}} = \hbar\omega_c c^\dagger c + \hbar\omega_m m^\dagger m + \hbar(gcm^\dagger + g^*c^\dagger m), \quad (1)$$

where $g/2\pi$ is the (complex) coherent coupling strength [40,41] between the cavity mode (operators c, c^\dagger) and the magnon mode (operators m, m^\dagger). The frequency of the cavity mode $\omega_c/2\pi$ is fixed by the cavity's geometry, while the ferromagnetic resonance of the magnon is tuned by a static magnetic field $\mathbf{H}_0 = H_0\hat{z}$ as $\omega_m = \gamma|\mathbf{H}_0|$, where $\gamma/2\pi = 28$ GHz/T is the gyromagnetic ratio.

The QLEs allow us to model the coupling of the cavity system described by Eq. (1) to the environment, to model intrinsic dissipation or external drives. To model the intrinsic damping of the cavity mode c and the magnon mode m , we assume that they each couple to a different bosonic bath with coupling constants $\kappa_c/2\pi$ and $\kappa_m/2\pi$. As per Fig. 1, the cavity system described by Eq. (1) is coupled to three ports p_i , $i = 1, 2, 3$, where the first two ports couple only to the cavity mode (with real-valued coupling constants $\kappa_1/2\pi$ and $\kappa_2/2\pi$ and phases ϕ_1, ϕ_2 [42]) and the third couples only to the magnon mode (real-valued coupling constant $\kappa_3/2\pi$ with phase ϕ_3). Physically, the coupling of the magnon to port 3 is due to the Zeeman interaction with the magnetic field created by the loop of port 3. The QLEs for the cavity and magnon modes then read (see

Appendix A for details)

$$\dot{c} = -i\tilde{\omega}_c c - ig^* m - \sqrt{\kappa_c} c^{\text{in}} - \sqrt{\kappa_1} e^{i\phi_1} p_1^{\text{in}} - \sqrt{\kappa_2} e^{i\phi_2} p_2^{\text{in}}, \quad (2)$$

$$\dot{m} = -i\tilde{\omega}_m m - igc - \sqrt{\kappa_m} m^{\text{in}} - \sqrt{\kappa_3} e^{i\phi_3} p_3^{\text{in}}, \quad (3)$$

where $\tilde{\omega}_c = \omega_c - i(\kappa_c + \kappa_1 + \kappa_2)/2$ and $\tilde{\omega}_m = \omega_m - i(\kappa_m + \kappa_3)/2$. In the QLEs, c^{in} and m^{in} account for intrinsic damping and have zero mean $\langle c^{\text{in}} \rangle = \langle m^{\text{in}} \rangle = 0$, while the p_i^{in} represent the inputs from the ports.

B. Two-tone reflection and transmission

We now assume that p_1^{in} and p_3^{in} correspond to coherent drives at the same frequency, albeit with a phase and amplitude difference written $\langle p_3^{\text{in}} \rangle = \delta e^{i\phi} \langle p_1^{\text{in}} \rangle$. We also perform a semiclassical approximation and neglect quantum fluctuations, which amounts to only considering expectation values. Using the input-output formalism (see Appendix B for details), the reflection at port 1 when port 3 is active is found to be

$$r_1(\omega) = \frac{\langle p_1^{\text{out}} \rangle |_{\langle p_2^{\text{in}} \rangle = 0}}{\langle p_1^{\text{in}} \rangle} \quad (4)$$

$$= 1 - i\sqrt{\kappa_1} \frac{\tilde{\Delta}_m \sqrt{\kappa_1} + g^* \sqrt{\kappa_3} e^{i(\phi_3 - \phi_1)} \delta e^{i\phi}}{\tilde{\Delta}_c \tilde{\Delta}_m - |g|^2}, \quad (5)$$

where $\tilde{\Delta}_c = \omega - \tilde{\omega}_c$ and $\tilde{\Delta}_m = \omega - \tilde{\omega}_m$. By comparing with the expressions of the standard S parameters (detailed in Appendix C), we note that the reflection r_1 can also be written $r_1(\omega) = S_{11} + \delta e^{i\phi} S_{13}$, which is expected given the linearity of the problem.

For $\delta \neq 0$, the reflection coefficient r_1 can be greater than 1, because it is only normalized to the input power from port 1, thus neglecting that of port 3. Following the setup of Fig. 1, and taking the power out of port 1 as a reference, the vector network analyzer outputs a power $1 + \delta^2$, so we can renormalize the reflection to $R_1(\omega) = 1/(\sqrt{1 + \delta^2}) r_1(\omega)$. Similarly, we can calculate the normalized transmission coefficient through port 2 when both port 1 and port 3 are active, and we find (Appendix D)

$$T_2(\omega) = \frac{1}{\sqrt{1 + \delta^2}} \frac{\langle p_2^{\text{out}} \rangle |_{\langle p_2^{\text{in}} \rangle = 0}}{\langle p_1^{\text{in}} \rangle} = \frac{S_{21} + \delta e^{i\phi} S_{23}}{\sqrt{1 + \delta^2}}. \quad (6)$$

We plot $|R_1|$ in Fig. 2 and $|T_2|$ in Fig. 3 with the parameters $\omega_c/2\pi = 10$ GHz, $|g|/2\pi = 20$ MHz, $\kappa_c/2\pi = \kappa_m/2\pi = 1$ MHz, $\kappa_1/2\pi = \kappa_2/2\pi = 10$ MHz, $\kappa_3/2\pi = 5$ MHz, $\varphi = \arg g = -\pi/2$, and $\phi_1 = \phi_2 = \phi_3 = 0$. The reflection R_1 exhibits controllable level repulsion and attraction depending on the amplitude δ of the drives and the dephasing ϕ , mirroring the experimental results of [31,32]. On the other hand, we notice that the transmission T_2 only shows

level repulsion, despite the system being driven in exactly the same way: between R_1 and T_2 , only the measurement location changes, and thus the physics should be the same. In the next section, we will attribute the observed level attraction to interference.

III. ANALYSIS AND VALIDATION BY FINITE-ELEMENT SIMULATIONS

A. Analysis of the two-tone reflection coefficient

An advantage of the input-output formalism is that it allows us to understand analytically the spectral features of Fig. 2. Indeed, by writing $r_1(\omega) = N(\omega)/D(\omega)$ in terms of a numerator N and a denominator D , the denominator can be factorized as

$$D(\omega) = \omega^2 - (\tilde{\omega}_c + \tilde{\omega}_m) \omega + \tilde{\omega}_c \tilde{\omega}_m - |g|^2 \quad (7)$$

$$= (\omega - \tilde{\omega}_+) (\omega - \tilde{\omega}_-), \quad (8)$$

where

$$\tilde{\omega}_{\pm} = \frac{\tilde{\omega}_c + \tilde{\omega}_m}{2} \pm \frac{\sqrt{(\tilde{\omega}_c - \tilde{\omega}_m)^2 + 4|g|^2}}{2} \quad (9)$$

are the complex-valued solutions of the quadratic Eq. (7).

On the other hand, the numerator N can be written as

$$N(\omega) = \omega^2 - (\tilde{\omega}'_c + \tilde{\omega}_m) \omega + \tilde{\omega}'_c \tilde{\omega}_m - G^2, \quad (10)$$

where we defined $\tilde{\omega}'_c = \tilde{\omega}_c + i\kappa_1$ and

$$G = |g| \sqrt{1 + \frac{\sqrt{\kappa_1 \kappa_3}}{|g|} \delta e^{i(\phi + \phi_3 - \phi_1 + \frac{\pi}{2} - \arg g)}}, \quad (11)$$

with $\arg g$ is the phase of the complex number g . Comparing Eqs. (7) and (10), we see that the numerator can be factored similarly to the denominator as $N(\omega) = (\omega - \tilde{\Omega}_+(\delta, \phi))(\omega - \tilde{\Omega}_-(\delta, \phi))$, where the complex frequencies $\tilde{\Omega}_{\pm}(\delta, \phi)$ are formally identical to Eq. (9), after replacing $\omega_c \mapsto \omega'_c$ and $|g| \mapsto G$. Finally, we obtain

$$r_1(\omega) = \frac{(\omega - \tilde{\Omega}_+(\delta, \phi)) (\omega - \tilde{\Omega}_-(\delta, \phi))}{(\omega - \tilde{\omega}_+) (\omega - \tilde{\omega}_-)}. \quad (12)$$

In general, the observed resonances and antiresonances of Eq. (12) are a combined effect of both the numerator N and the denominator D . However, as discussed below, and numerically illustrated in Fig. 2, the spectral features are well characterized by the poles (zeros $\tilde{\omega}_{\pm}$ of D) and zeros (zeros $\tilde{\Omega}_{\pm}$ of N) of r_1 . Notably, it is sufficient to solely examine the zeros $\tilde{\Omega}_{\pm}$ to understand the resonances, and the poles $\tilde{\omega}_{\pm}$ to understand the antiresonances, independently of each other.

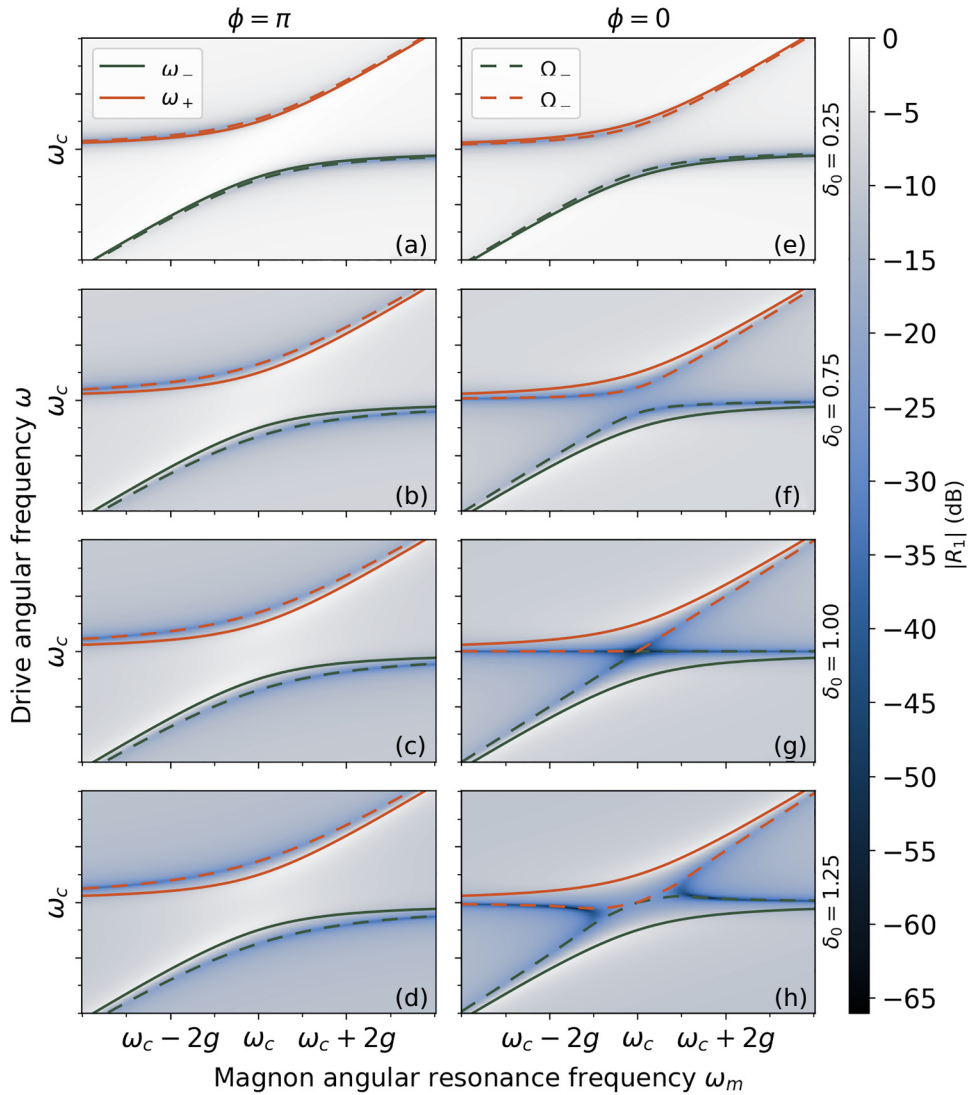


FIG. 2. Normalized reflection amplitude $|R_1|$ at port 1 for increasing values of $\delta_0 = \sqrt{\kappa_1 \kappa_3} / (|g|) \delta$ from top to bottom, and a dephasing $\phi = \pi$ (first column) and $\phi = 0$ (second column) between the drives of port 1 and port 3. The solid lines correspond to the real part of the zeros $\tilde{\omega}_\pm$ of the denominator of R_1 , given by Eq. (9), while the dashed lines correspond to the zeros $\tilde{\Omega}_\pm$ of the numerator of R_1 .

For small dissipation rates κ_i , the imaginary part of $\tilde{\omega}_\pm$ is small compared to its real part. Therefore, in Eq. (12), when ω is close to $\omega_\pm = \text{Re}\{\tilde{\omega}_\pm\}$, the denominator $|D|$ of $|R_1|$ almost vanishes, leading to a resonance behavior (maxima) of $|R_1|$. Furthermore, ω_\pm corresponds to the spectrum of the Hamiltonian of Eq. (1), and hence this resonance behavior is expected to give information about the spectrum of the closed system. As shown by the solid lines in Figs. 2 and 3, the spectrum is that of coherent coupling, characterized by energy level repulsion with an angular frequency gap $2|g|$. Hence, the denominator of $|R_1|$, or equivalently its resonances, does inform on the underlying physics.

The situation is different for the numerator N of R_1 , which leads to antiresonances. Indeed, while the

expressions for $\tilde{\omega}_\pm$ and $\tilde{\Omega}_\pm$ are formally identical, the antiresonance coupling strength $G/2\pi$ for $\tilde{\Omega}_\pm$ is complex-valued (while it is real-valued, $|g|/2\pi$, for $\tilde{\omega}_\pm$), which can lead to level attraction. To see this more clearly, it is convenient to introduce the effective amplitude $\delta_0 = \sqrt{\kappa_1 \kappa_3} / (|g|) \delta$ and the effective phase $\phi_0 = \phi_1 - \phi_3 + \arg g - \pi/2$ of port 3. We can then rewrite Eq. (11) as

$$G = g \sqrt{1 + \delta_0 e^{i(\phi - \phi_0)}}. \quad (13)$$

Therefore, when $\phi - \phi_0 = 0$ the antiresonance coupling strength $G/2\pi$ is real-valued and increases as δ_0 increases, leading to an increase in level repulsion (see the dashed lines in the first column of Fig. 2). On the other hand, when $\phi - \phi_0 = \pi$, $G/2\pi$ is real-valued when $\delta_0 < 1$ and

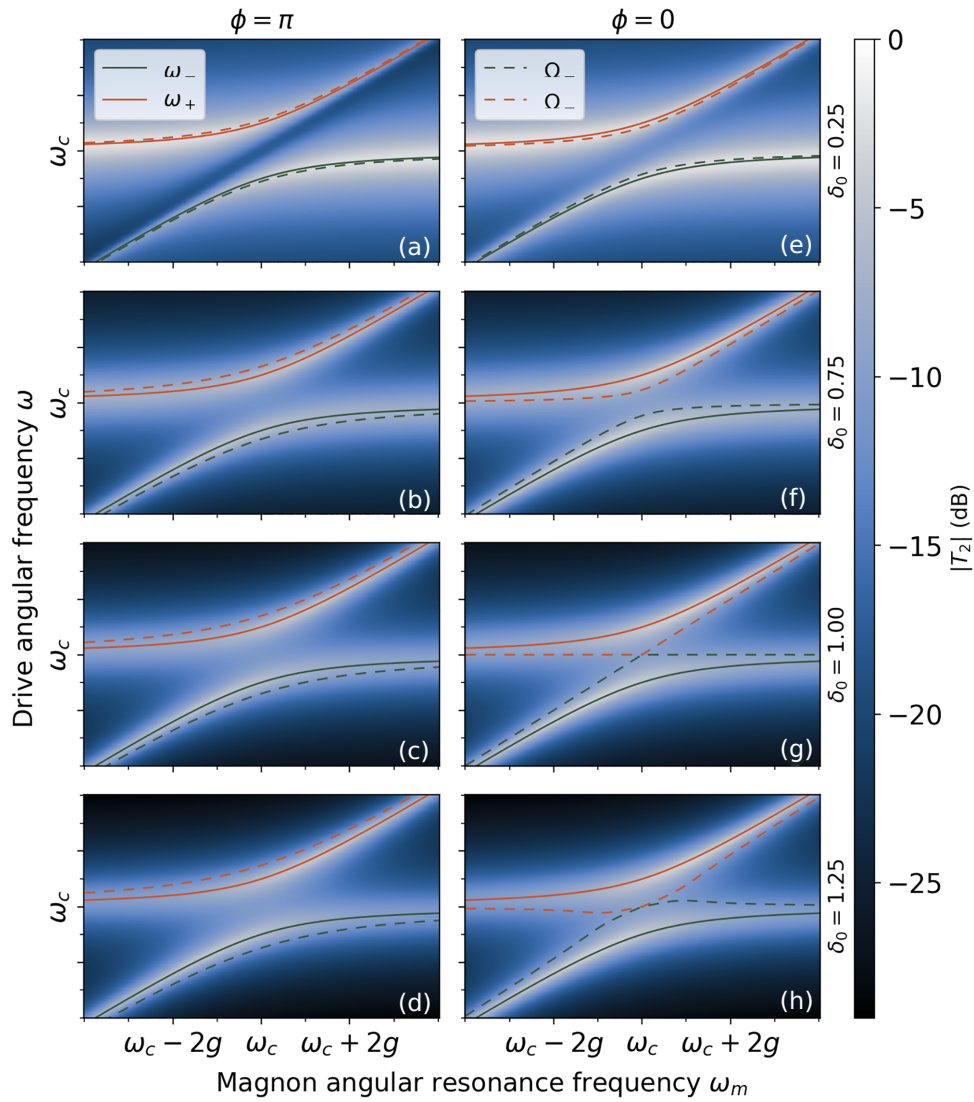


FIG. 3. Normalized transmission amplitude $|T_2|$ through port 2 for $\phi = \pi$ and $\phi = 0$, and increasing values of δ_0 from top to bottom. The parameters and legends used are identical to those of Fig. 2.

diminishes when δ_0 increases. Eventually, when $\delta_0 > 1$, the $G/2\pi$ becomes purely imaginary due to taking the square root of a negative number, leading to level attraction. In the limiting case where $\delta_0 = 1$, we have $G = 0$ and we obtain two uncoupled antiresonances as shown in Fig. 2(g) (horizontal at the cavity mode frequency and diagonal at the magnon's frequency $\omega_m/2\pi$). As can be seen from the dashed lines in Fig. 2, these spectral features indeed correspond to antiresonances (minima of $|R_1|$) at the frequencies Ω_{\pm} . Physically, these frequencies Ω_{\pm} are determined by the interference between the numerators of S_{11} and S_{13} since $r_1(\omega) = S_{11} + \delta e^{i\phi} S_{13}$. Hence, the input-output formalism shows that while the denominator of $|R_1|$ informs on the physics, the numerator is interference-based. Furthermore, the denominators of both

R_1 and T_2 are identical (see Appendix D for the detailed expression), leading to similar resonant behavior following the coherent coupling spectrum. However, their antiresonance behaviors differ because their numerators differ (see Appendix D).

Concerning the occurrence of level attraction, we note that it requires the total phase $\phi + \phi_3 - \phi_1 + \pi/2 - \arg g$ to be equal to π . Physically, this is determined by the magnon-photon coupling phase $\arg g$, the coupling of the cavity and magnon modes to the probes (ϕ_1 and ϕ_3), and the chosen phase difference ϕ between port 1 and port 3. The strength of level attraction itself is determined by $|G|$, which depends on $|g|$ and the ratio $\sqrt{\kappa_1 \kappa_3}/g$ (i.e., the magnon-photon coupling strength and the coupling to the ports).

B. Numerical finite-element results

The input-output formalism provides interesting insights thanks to the resulting analytical expressions. However, it remains a toy model of a two-tone driving experiment. Instead, a realistic modeling, taking into account the geometry of the cavity and of the ports, can be performed using COMSOL MULTIPHYSICS[®], a finite-element modeling program. We use a two-post re-entrant cavity [43,44], similar to that sketched in Fig. 1, in which the loop antenna of port 3 is inserted from the bottom of the cavity (see Appendix H for more details). At the location of the YIG sphere, the cavity mode's magnetic field is purely along the \hat{x} axis [39]. In our analysis, we assumed that port 3 does not couple to the cavity mode, which requires us to orient the loop antenna so that it generates a magnetic field orthogonal to the cavity mode. Thus, denoting by $\hat{\mathbf{n}}$ the normal to the plane of the loop, we need $\hat{\mathbf{n}}$ to be in the x - z plane. Furthermore, since only the components orthogonal to the static magnetic field $H_0\hat{\mathbf{z}}$ contribute to the coupling between port 3 and the magnon, $\kappa_3/2\pi$ is maximum when $\hat{\mathbf{n}} = \hat{\mathbf{y}}$.

We first numerically calculated the S parameters for different values of \mathbf{H}_0 using COMSOL MULTIPHYSICS[®], as detailed in Appendix H. From these two S parameters, we can plot R_1 and T_2 after normalizing $r_1(\omega) = S_{11} + \delta e^{i\phi} S_{13}$ and $t_2(\omega) = S_{21} + \delta e^{i\phi} S_{23}$, and we obtain the results of Fig. 4, which successfully reproduce the input-output theory results of Figs. 2 and 3. As a further verification, we also performed a fully two-tone experiment in COMSOL MULTIPHYSICS[®] for $\delta = 12$, and the results were identical to those of the second and fourth rows of Fig. 4.

IV. PHYSICAL INTERPRETATION

In Secs. II and III, we considered the experimentally accessible observables, that is, the reflection and transmission amplitudes. We confirmed that the resonances of R_1 and T_2 follow energy level repulsion, suggesting coherent coupling physics. As the same time, we saw that the antiresonances of R_1 can lead to level attraction, which begs the question of what physics is effectively taking place. The physics can be inferred from the dynamics of the cavity and magnon modes in the presence of the two coherent drives, given by the QLEs. Therefore, to derive the effective Hamiltonian, we write the QLEs [Eqs. (2) and (3)] in the semiclassical approximation where operators are replaced by their expectation values. Recalling that $\langle c^{\text{in}} \rangle = \langle m^{\text{in}} \rangle = 0$, the QLEs read

$$\dot{c} = -i\tilde{\omega}_c c - igm - \sqrt{\kappa_1} e^{i\phi_1} p_1^{\text{in}} - \sqrt{\kappa_2} e^{i\phi_2} p_2^{\text{in}}, \quad (14)$$

$$\dot{m} = -i\tilde{\omega}_m m - igc - \sqrt{\kappa_3} e^{i\phi_3} p_3^{\text{in}}. \quad (15)$$

In both a reflection and transmission measurement, port 2 is not driven, so we set $p_2^{\text{in}} = 0$. On the other hand, p_1^{in} and p_3^{in} correspond to coherent drives at frequency

$\omega/2\pi$ with amplitudes \mathcal{E} and $\delta e^{i\phi} \mathcal{E}$. Thus, further defining $\mathcal{E}_1 = \sqrt{\kappa_1/2\pi} e^{i\phi_1} \mathcal{E}$ and $\mathcal{E}_3 = \sqrt{\kappa_3/2\pi} e^{i\phi_3} \mathcal{E} \delta e^{i\phi}$, the QLEs become, from Appendix B,

$$\dot{c} = -i\tilde{\omega}_c c - igm - \mathcal{E}_1 e^{-i\omega t}, \quad (16)$$

$$\dot{m} = -i\tilde{\omega}_m m - igc - \mathcal{E}_3 e^{-i\omega t}. \quad (17)$$

From these equations, we find that the effective non-hermitian Hamiltonian (recall that $\tilde{\omega}_c, \tilde{\omega}_m \in \mathbb{C}$)

$$H_{\text{eff}} = \hbar\tilde{\omega}_c c^\dagger c + \hbar\tilde{\omega}_m m^\dagger m + \hbar(gcm^\dagger + g^* c^\dagger m) + i\hbar(\mathcal{E}_1 c e^{i\omega t} - \text{h.c.}) + i\hbar(\mathcal{E}_3 m e^{i\omega t} - \text{h.c.}) \quad (18)$$

where h.c. stands for the hermitian conjugate terms, gives Heisenberg equations of motion identical to Eqs. (16) and (17). Thus, the physics described by Eq. (18) is identical to that given by the QLEs. After a rotating frame transformation to remove the time dependence and displacement operations (see Appendix G for details), this Hamiltonian is unitarily equivalent to

$$H'_{\text{eff}} = -\hbar\tilde{\Delta}_c c^\dagger c - \hbar\tilde{\Delta}_m m^\dagger m + \hbar(gcm^\dagger + g^* c^\dagger m). \quad (19)$$

Formally similar to the closed-system Hamiltonian of Eq. (1), this effective Hamiltonian describes a coherent coupling physics, with a spectrum corresponding to level repulsion. Since H'_{eff} describes the physics of the cavity system in the presence of coherent drives, we conclude that the physics of two-tone driving indeed corresponds to coherent coupling, even though the reflection coefficient can show level attraction due to interference-based antiresonances. Therefore, the antiresonance frequencies $\Omega_\pm/2\pi$ (dashed lines in Fig. 2) do not correspond to the spectrum of the system, which are instead given by $\omega_\pm/2\pi$ (solid lines in Fig. 2). Notably, the antiresonance coupling $G/2\pi$ is merely a convenient quantity to understand the attraction and repulsion of the antiresonances, but it does not represent a physical coupling. For instance, when $\delta_0 = 1$, the magnon and cavity modes are still coherently coupled with coupling strength $g/2\pi$, even though $G = 0$ and level crossing is observed [see Fig. 2(g)].

In the two-tone driving system studied here, the antiresonances leading to level attraction come from interferences between S_{11} and S_{13} , but antiresonances can also appear in one-tone-driven systems as experimentally demonstrated by Rao *et al.* [45]. Notably, these antiresonances can exhibit different coupling behavior as recently analyzed by [42], and suggest energy level repulsion and attraction with a magnon mode. These behaviors are associated with the numerators of the transmission coefficient, and therefore they are not associated to a physical coherent and dissipative coupling (even though they do allow experimental data to be fitted). Importantly, it is incorrect to derive an effective Hamiltonian from this numerator alone, as it is not associated with a physical dynamics.

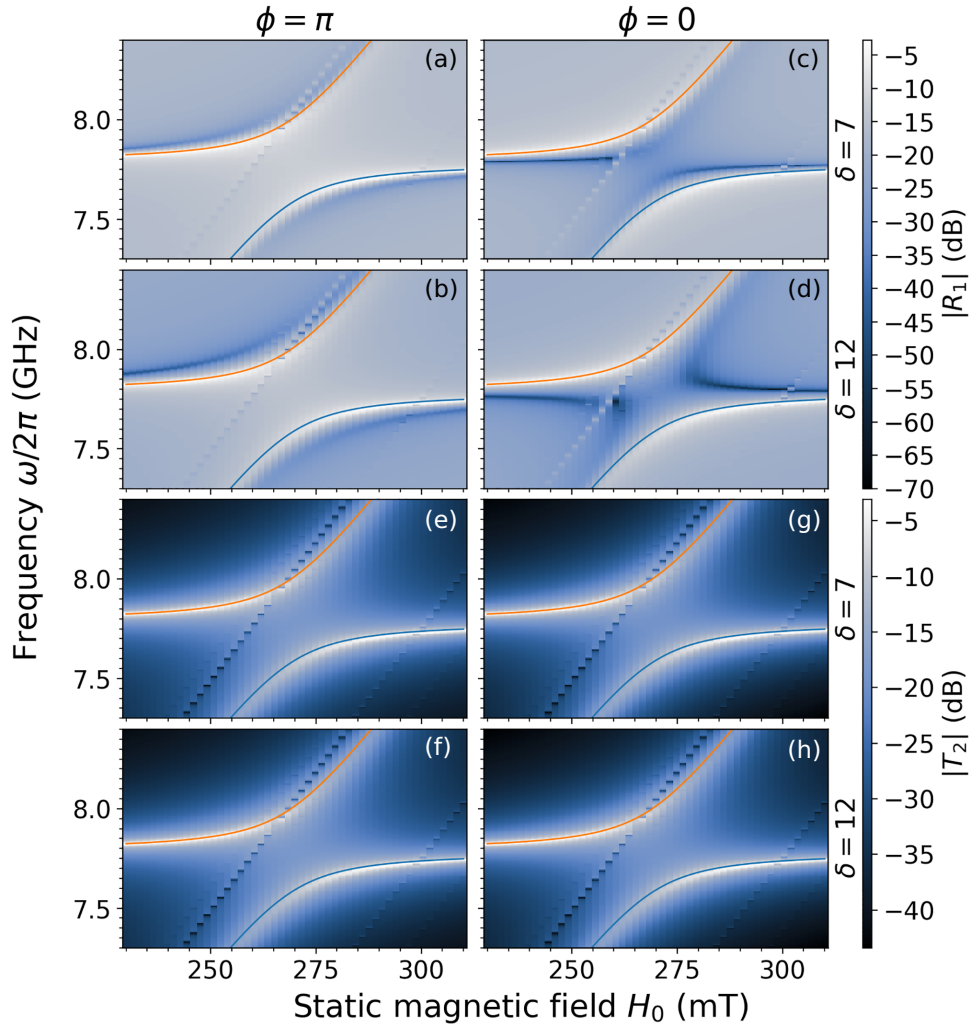


FIG. 4. Plots of the normalized reflection and transmission amplitudes $|R_1|, |T_2|$ using the numerical values of the S parameters obtained using COMSOL MULTIPHYSICS[®]. Note that, contrary to Fig. 2, we varied the amplitude δ at port 3 instead of the effective amplitude δ_0 , because the latter depends on the unknown parameters κ_1, κ_3 .

V. CONCLUSION

To conclude, we have shown that when two bosonic modes are simultaneously driven, the resonances in reflection and transmission indeed inform on the normal modes of the system, while the observed antiresonances in reflection are due to interference physics, and are unrelated to the normal modes of the coupled system. Therefore, there is no dissipative coupling physics in this system, which makes the two-tone driving scheme unsuitable for the *in situ* control of coherent and dissipative couplings. Still, realizing such an all-microwave control remains a relevant research direction, due to the promising applications it would unlock.

It is worth mentioning that an interference-based level attraction was recently used in a cavity magnonics system to experimentally achieve a nearly perfect single-beam

absorption of 96% [46]. However, it once again required a vector magnet, whereas in the present work we achieved similar physics through a flexible two-tone driving instead. Thus, it is of interest to explore the possibilities offered by two-tone driving for coherent perfect absorption, which we leave for future work.

Finally, while we considered a cavity magnonics system as a physical realization of two coupled bosonic modes, many other systems, such as intersubband polaritons [47] or cavity optomechanics in the red-detuned regime [48], reduce to a similar Hamiltonian (the Dicke model [49] after employing the Holstein-Primakoff transformation [50] and the rotating wave approximation [51]). While the details of how such modes would be coherently driven would differ, the derivations employed here are very general and may prove useful to analyze the physics in other open systems.

ACKNOWLEDGMENTS

We acknowledge financial support from Thales Australia and Thales Research and Technology. This work is part of the research program supported by the European Union through the European Regional Development Fund (ERDF), by the Ministry of Higher Education and Research, Brittany and Rennes Métropole, through the CPER SpaceTech DroneTech, by Brest Métropole, and the ANR projects ICARUS (ANR-22-CE24-0008) and MagFunc (ANR-20-CE91-0005). The scientific color map *oslo* [52] was used to prevent visual distortion of the data and exclusion of readers with colorvision deficiencies [53].

APPENDIX A: DERIVATION OF THE QUANTUM LANGEVIN EQUATIONS

1. System definition

In this appendix, we derive the QLEs of the coupled magnon-photon cavity system under the rotating wave approximation, which is valid for $|g| \ll \omega_c, \omega_m$ [51,54], where $g/2\pi$ is the coupling strength. We recall that the most general Hamiltonian describing a coupled magnon-photon system reads [40]

$$H_{\text{sys}} = \hbar\omega_c c^\dagger c + \hbar\omega_m m^\dagger m + \hbar(gcm^\dagger + g^*c^\dagger m), \quad (\text{A1})$$

where $g/2\pi$ is complex-valued due to potential coupling phases [41].

The intrinsic losses of the cavity and magnon modes (respectively due to radiative losses and Gilbert damping) can be modeled by coupling to two bosonic baths described by the Hamiltonians

$$H_{\text{bath,intrinsic}} = \int_{\mathbb{R}} d\omega \hbar\omega a_\omega^\dagger a_\omega + \int_{\mathbb{R}} d\omega \hbar\omega b_\omega^\dagger b_\omega, \quad (\text{A2})$$

$$H_{\text{cav-bath,intrinsic}} = \int_{\mathbb{R}} d\omega i\hbar \sqrt{\frac{\kappa_c}{2\pi}} (ca_\omega^\dagger - c^\dagger a_\omega) + \int_{\mathbb{R}} d\omega i\hbar \sqrt{\frac{\kappa_m}{2\pi}} (cb_\omega^\dagger - c^\dagger b_\omega). \quad (\text{A3})$$

Here, we have assumed frequency-independent (Markov approximation) and real-valued coupling rates $\kappa_c/2\pi, \kappa_m/2\pi$ to the baths.

Additionally, the cavity system is coupled to the environment through three ports, used to inject and sense microwave fields. We label them as port 1, port 2, and port 3. To model the coupling of the magnon and cavity modes to the ports, we again couple them to a bosonic bath, but this time we allow the coupling rates to be complex-valued

to model potential dephasing of the microwaves through the coaxial cables or due to the antenna geometry [42]. Therefore, we assume that the cavity mode couples to ports 1 and 2 with coupling constants $\kappa_1/2\pi, \kappa_2/2\pi$, and phases ϕ_1, ϕ_2 , while the magnon couples to port 3 only, with coupling constant $\kappa_3/2\pi$ and phase ϕ_3 . For the sake of completeness, we further consider that the cavity mode can couple to port 3 with coupling constant $\zeta\kappa_3/2\pi$ and phase ϕ'_3 , where ζ is a dimensionless constant. The continuous-frequency bosonic bath of port i is described by creation and annihilation operators $p_{i,\omega}^\dagger, p_{i,\omega}$ with Hamiltonian

$$H_{\text{bath,ports}} = \sum_{i=1}^3 \int_{\mathbb{R}} d\omega \hbar\omega p_{i,\omega}^\dagger p_{i,\omega}, \quad (\text{A4})$$

while the interaction between the bath and the cavity system is modeled by

$$H_{\text{cav-bath,ports}} = \int_{\mathbb{R}} d\omega i\hbar \sqrt{\frac{\kappa_1}{2\pi}} (cp_{1,\omega}^\dagger e^{-i\phi_1} - c^\dagger p_{1,\omega} e^{i\phi_1}) + \int_{\mathbb{R}} d\omega i\hbar \sqrt{\frac{\kappa_2}{2\pi}} (cp_{2,\omega}^\dagger e^{-i\phi_2} - c^\dagger p_{2,\omega} e^{i\phi_2}) + \int_{\mathbb{R}} d\omega i\hbar \sqrt{\frac{\kappa_3}{2\pi}} (mp_{3,\omega}^\dagger e^{-i\phi_3} - m^\dagger p_{3,\omega} e^{i\phi_3}) + \int_{\mathbb{R}} d\omega i\hbar \sqrt{\frac{\zeta\kappa_3}{2\pi}} (cp_{3,\omega}^\dagger e^{-i\phi_3} - c^\dagger p_{3,\omega} e^{i\phi'_3}). \quad (\text{A5})$$

Thus, the total Hamiltonian of the joint cavity system and environment is

$$H = H_{\text{sys}} + H_{\text{bath,intrinsic}} + H_{\text{cav-bath,intrinsic}} + H_{\text{bath,ports}} + H_{\text{cav-bath,ports}}. \quad (\text{A6})$$

2. Equations of motion

The Heisenberg equation of motion for $p_{1,\omega}$ is

$$\dot{p}_{1,\omega}(t) = -i\omega p_{1,\omega}(t) + \sqrt{\frac{\kappa_1}{2\pi}} e^{-i\phi_1} c(t). \quad (\text{A7})$$

The formal solution for an arbitrary $t_0 < t$ is

$$p_{1,\omega}(t) = e^{-i\omega(t-t_0)} p_{1,\omega}(t_0) + \int_{t_0}^t dt' \sqrt{\frac{\kappa_1}{2\pi}} e^{-i\phi_1} c(t') e^{-i\omega(t-t')}, \quad (\text{A8})$$

and by analogy we deduce that

$$p_{2,\omega}(t) = e^{-i\omega(t-t_0)} p_{2,\omega}(t_0) + \int_{t_0}^t dt' \sqrt{\frac{\kappa_2}{2\pi}} e^{-i\phi_2} c(t') e^{-i\omega(t-t')}, \quad (\text{A9})$$

$$p_{3,\omega}(t) = e^{-i\omega(t-t_0)} p_{3,\omega}(t_0) + \int_{t_0}^t dt' \sqrt{\frac{\kappa_3}{2\pi}} e^{-i\phi_3} m(t') e^{-i\omega(t-t')} + \int_{t_0}^t dt' \sqrt{\frac{\zeta \kappa_3}{2\pi}} e^{-i\phi'_3} c(t') e^{-i\omega(t-t')}, \quad (\text{A10})$$

$$a_\omega(t) = e^{-i\omega(t-t_0)} a_\omega(t_0) + \int_{t_0}^t dt' \sqrt{\frac{\kappa_c}{2\pi}} c(t') e^{-i\omega(t-t')}, \quad (\text{A11})$$

$$b_\omega(t) = e^{-i\omega(t-t_0)} b_\omega(t_0) + \int_{t_0}^t dt' \sqrt{\frac{\kappa_m}{2\pi}} m(t') e^{-i\omega(t-t')}. \quad (\text{A12})$$

Taking $t_0 \rightarrow -\infty$ and using $\int_{-\infty}^t dt' f(t') \delta(t-t') = \frac{1}{2} f(t)$, the Heisenberg equation of motion for m is

$$\begin{aligned} \dot{m}(t) &= -i\omega_m m(t) - igc(t) - \sqrt{\frac{\kappa_m}{2\pi}} \int_{\mathbb{R}} d\omega b_\omega(t) - \sqrt{\frac{\kappa_3}{2\pi}} e^{i\phi_3} \int_{\mathbb{R}} d\omega p_{3,\omega}(t) \\ &= -i\omega_m m(t) - igc(t) - \sqrt{\kappa_m} m^{\text{in}}(t) - \frac{\kappa_m}{2\pi} \int_{t_0 \rightarrow -\infty}^t dt' m(t') \int_{\mathbb{R}} d\omega e^{-i\omega(t-t')} \\ &\quad - \sqrt{\kappa_3} e^{i\phi_3} p_3^{\text{in}}(t) - \frac{\kappa_3}{2\pi} \int_{t_0 \rightarrow -\infty}^t dt' \left(m(t') + e^{i(\phi_3 - \phi'_3)} \sqrt{\zeta} c(t') \right) 2\pi \delta(t-t') \\ &= -i\tilde{\omega}_m m(t) - \left(ig + e^{i(\phi_3 - \phi'_3)} \sqrt{\zeta} \frac{\kappa_3}{2} \right) c(t) - \sqrt{\kappa_m} m^{\text{in}}(t) - \sqrt{\kappa_3} e^{i\phi_3} p_3^{\text{in}}(t), \end{aligned} \quad (\text{A13})$$

with $\tilde{\omega}_m = \omega_m - i(\kappa_m + \kappa_3)/2$,

$$p_i^{\text{in}}(t) = \lim_{t_0 \rightarrow -\infty} \frac{1}{\sqrt{2\pi}} \int_{\mathbb{R}} d\omega e^{-i\omega(t-t_0)} p_{i,\omega}(t_0), \quad (\text{A14})$$

and

$$\begin{aligned} c^{\text{in}}(t) &= \lim_{t_0 \rightarrow -\infty} \frac{1}{\sqrt{2\pi}} \int_{\mathbb{R}} d\omega e^{-i\omega(t-t_0)} a_\omega(t_0), \\ m^{\text{in}}(t) &= \lim_{t_0 \rightarrow -\infty} \frac{1}{\sqrt{2\pi}} \int_{\mathbb{R}} d\omega e^{-i\omega(t-t_0)} b_\omega(t_0). \end{aligned} \quad (\text{A15})$$

Note that we defined the input fields following the original convention of [38], but a different choice, with a minus sign instead, can also be made. This only changes the phase reference for the ports, and does not impact our results. Indeed, one can formally check that changing $p_i^{\text{in}} \mapsto -p_i^{\text{in}}$ implies $\tilde{c} \mapsto -\tilde{c}$ [see, for example, Eq. (B7)]. As a consequence, one finds that $r_1 \mapsto -r_1$ and $t_2 \mapsto -t_2$, leading to a phase shift of π which is unobservable when considering the reflection and transmission amplitudes.

Similarly, the Heisenberg equation of motion for c reads

$$\begin{aligned} \dot{c}(t) &= -i\omega_c c(t) - ig^* m(t) - \sqrt{\frac{\kappa_c}{2\pi}} \int_{\mathbb{R}} d\omega a_\omega(t) \\ &\quad - \sqrt{\frac{\kappa_1}{2\pi}} e^{i\phi_1} \int_{\mathbb{R}} d\omega p_{1,\omega}(t) - \sqrt{\frac{\kappa_2}{2\pi}} e^{i\phi_2} \int_{\mathbb{R}} d\omega p_{2,\omega}(t) - \sqrt{\frac{\zeta \kappa_3}{2\pi}} e^{i\phi'_3} \int_{\mathbb{R}} d\omega p_{3,\omega}(t) \\ &= -i\omega_c c(t) - ig^* m(t) - e^{i(\phi'_3 - \phi_3)} \sqrt{\zeta} \frac{\kappa_3}{2} m(t) - \frac{\kappa_c + \kappa_1 + \kappa_2 + \zeta \kappa_3}{2} c(t) \\ &\quad - \sqrt{\kappa_c} c^{\text{in}}(t) - \sqrt{\kappa_1} e^{i\phi_1} p_1^{\text{in}}(t) - \sqrt{\kappa_2} e^{i\phi_2} p_2^{\text{in}}(t) - \sqrt{\zeta \kappa_3} e^{i\phi'_3} p_3^{\text{in}}(t) \\ &= -i\tilde{\omega}_c c(t) - \tilde{g}^* m(t) - \sqrt{\kappa_c} c^{\text{in}}(t) - \sqrt{\kappa_1} e^{i\phi_1} p_1^{\text{in}}(t) - \sqrt{\kappa_2} e^{i\phi_2} p_2^{\text{in}}(t) - \sqrt{\zeta \kappa_3} e^{i\phi'_3} p_3^{\text{in}}(t). \end{aligned} \quad (\text{A16})$$

where we defined $\tilde{\omega}_c = \omega_c - i(\kappa_c + \kappa_1 + \kappa_2 + \zeta\kappa_3)/2$ and $\tilde{g}' = g^* - i\sqrt{\zeta}\frac{\kappa_3}{2}e^{i(\phi_3' - \phi_3)}$. Similarly defining $\tilde{g} = g - i\sqrt{\zeta}\frac{\kappa_3}{2}e^{i(\phi_3 - \phi_3')}$, we can rewrite the Heisenberg equations of motion as

$$\dot{m} = -i\tilde{\omega}_m m - \tilde{g}c - \sqrt{\kappa_m}m^{\text{in}}(t) - \sqrt{\kappa_3}e^{i\phi_3}p_3^{\text{in}}(t), \quad (\text{A17})$$

$$\begin{aligned} \dot{c} = & -i\tilde{\omega}_c c - \tilde{g}'m - \sqrt{\kappa_c}c^{\text{in}}(t) - \sqrt{\kappa_1}e^{i\phi_1}p_1^{\text{in}}(t) \\ & - \sqrt{\kappa_2}e^{i\phi_2}p_2^{\text{in}}(t) - \sqrt{\zeta}\kappa_3e^{i\phi_3'}p_3^{\text{in}}(t), \end{aligned} \quad (\text{A18})$$

which are the QLEs given in the main text.

APPENDIX B: CALCULATION OF THE REFLECTION AT PORT 1

1. Frequency-space solutions

We now perform a semiclassical approximation, and replace operators by their expectation value. Recalling that $\langle c^{\text{in}} \rangle = \langle m^{\text{in}} \rangle = 0$, the QLEs simplify to

$$\dot{m} = -i\tilde{\omega}_m m - \tilde{g}c - \sqrt{\kappa_3}e^{i\phi_3}p_3^{\text{in}}(t), \quad (\text{B1})$$

$$\begin{aligned} \dot{c} = & -i\tilde{\omega}_c c - \tilde{g}'m - \sqrt{\kappa_1}e^{i\phi_1}p_1^{\text{in}}(t) - \sqrt{\kappa_2}e^{i\phi_2}p_2^{\text{in}}(t) \\ & - \sqrt{\zeta}\kappa_3e^{i\phi_3'}p_3^{\text{in}}(t), \end{aligned} \quad (\text{B2})$$

and in frequency space,

$$-i\omega\tilde{m} = -i\tilde{\omega}_m\tilde{m} - \tilde{g}\tilde{c} - \sqrt{\kappa_3}e^{i\phi_3}\tilde{p}_3^{\text{in}}, \quad (\text{B3})$$

$$\begin{aligned} -i\tilde{\Delta}_c\tilde{c} = & -\tilde{g}'\tilde{m} - \sqrt{\kappa_1}e^{i\phi_1}\tilde{p}_1^{\text{in}} - \sqrt{\kappa_2}e^{i\phi_2}\tilde{p}_2^{\text{in}} \\ & - \sqrt{\zeta}\kappa_3e^{i\phi_3'}\tilde{p}_3^{\text{in}}, \end{aligned} \quad (\text{B4})$$

with $\tilde{\Delta}_c = \omega - \tilde{\omega}_c$ and $\tilde{\Delta}_m = \omega - \tilde{\omega}_m$. In particular, the first equation gives

$$\tilde{m} = \frac{\tilde{g}\tilde{c} - i\sqrt{\kappa_3}e^{i\phi_3}\tilde{p}_3^{\text{in}}}{\tilde{\Delta}_m}, \quad (\text{B5})$$

which, inserted in the second equation, leads to

$$\tilde{c} = \frac{\tilde{g}'\tilde{m} - i\sqrt{\kappa_1}e^{i\phi_1}\tilde{p}_1^{\text{in}} - i\sqrt{\kappa_2}e^{i\phi_2}\tilde{p}_2^{\text{in}} - i\sqrt{\zeta}\kappa_3e^{i\phi_3'}\tilde{p}_3^{\text{in}}}{\tilde{\Delta}_c} \quad (\text{B6})$$

$$\begin{aligned} = & \frac{-i}{A(\omega)} \left[\tilde{\Delta}_m\sqrt{\kappa_1}e^{i\phi_1}\tilde{p}_1^{\text{in}} + \tilde{\Delta}_m\sqrt{\kappa_2}e^{i\phi_2}\tilde{p}_2^{\text{in}} \right. \\ & \left. + \left(\tilde{g}'e^{i\phi_3} + \sqrt{\zeta}e^{i\phi_3'}\tilde{\Delta}_m \right) \sqrt{\kappa_3}\tilde{p}_3^{\text{in}} \right], \end{aligned}$$

where $A(\omega) = \tilde{\Delta}_c\tilde{\Delta}_m - \tilde{g}\tilde{g}'$.

2. Input-output relations

To derive the input-output relations, we first write the formal solution of $p_{1,\omega}$ for $t < t_1$ as

$$\begin{aligned} p_{1,\omega}(t) = & e^{-i\omega(t-t_1)}p_{1,\omega}(t_1) \\ & - \int_t^{t_1} dt' \sqrt{\frac{\kappa_1}{2\pi}} e^{-i\phi_1}c(t')e^{-i\omega(t-t')}, \end{aligned} \quad (\text{B7})$$

and we have on the one hand

$$\int_{\mathbb{R}} d\omega p_{1,\omega}(t) = \sqrt{2\pi} \left(p_1^{\text{in}}(t) + \frac{\sqrt{\kappa_1}}{2} e^{-i\phi_1}c(t) \right), \quad (\text{B8})$$

and on the other

$$\int_{\mathbb{R}} d\omega p_{1,\omega}(t) = \sqrt{2\pi} \left(p_{1,\omega}^{\text{out}}(t) - \frac{\sqrt{\kappa_1}}{2} e^{-i\phi_1}c(t) \right), \quad (\text{B9})$$

so that the input-output relation is

$$p_1^{\text{out}}(t) = p_1^{\text{in}}(t) + \sqrt{\kappa_1}e^{-i\phi_1}c(t). \quad (\text{B10})$$

We can similarly derive

$$p_2^{\text{out}}(t) = p_2^{\text{in}}(t) + \sqrt{\kappa_2}e^{-i\phi_2}c(t), \quad (\text{B11})$$

$$p_3^{\text{out}}(t) = p_3^{\text{in}}(t) + \sqrt{\kappa_3}e^{-i\phi_3}m(t) + \sqrt{\zeta}\kappa_3e^{-i\phi_3'}c(t). \quad (\text{B12})$$

3. Modeling coherent drives

To examine the reflection and transmission, we consider that p_1 , coupling to the cavity mode, is a coherent drive at frequency $\omega_d/2\pi$. Such a coherent drive is expected to reproduce the classical dynamics through the use of coherent states [55]. Formally, the state space for p_1 is the product of the Fock space of the bath operators $p_{1,\omega}$ for each frequency $\omega/2\pi$. Formally, the state of the bath is the tensor product $\bigotimes_{\omega \in \mathbb{R}} |\psi_\omega\rangle$, where $|\psi_\omega\rangle$ is the state of the bosonic mode described by the annihilation operator $p_{1,\omega}$. If we assume a coherent drive, then only the mode of frequency $\omega_d/2\pi$ has a nonvanishing number of excitations, which we take to be a coherent state $|\mathcal{E}_{\omega_d}\rangle$. Formally, $|\psi_\omega\rangle = |0\rangle$ if $\omega \neq \omega_d$, and $|\psi_\omega\rangle = |\mathcal{E}_{\omega_d}\rangle$ if $\omega = \omega_d$. Hence, $\langle p_1 \rangle = \langle \mathcal{E}_{\omega_d} | p_1 | \mathcal{E}_{\omega_d} \rangle = \mathcal{E}_{\omega_d} \in \mathbb{C}$, since we recall that coherent states are eigenstates of annihilation operators [55]. We make a similar approximation for port 3 driving the magnon, albeit with a different amplitude and phase, and hence $\langle p_3 \rangle = \delta e^{i\phi} \mathcal{E}_{\omega_d}$.

A convenient choice for the coherent state \mathcal{E}_{ω_d} is $\mathcal{E}_{\omega_d} = \lim_{t_0 \rightarrow -\infty} \alpha e^{-i\omega_d t_0}$, with $\mathcal{E} \in \mathbb{R}$. Indeed, in the time domain this gives, for instance,

$$\begin{aligned}
\langle p_1^{\text{in}}(t) \rangle &= \langle \mathcal{E}_{\omega_d} | p_1^{\text{in}}(t) | \mathcal{E}_{\omega_d} \rangle \\
&= \lim_{t_0 \rightarrow -\infty} \langle \alpha e^{i\omega_d t_0} | \frac{1}{\sqrt{2\pi}} \int_{\mathbb{R}} d\omega e^{-i\omega(t-t_0)} p_{1,\omega}(t_0) | \mathcal{E} e^{-i\omega_d t_0} \rangle \\
&= \lim_{t_0 \rightarrow -\infty} \langle \mathcal{E} e^{i\omega_d t_0} | \frac{1}{\sqrt{2\pi}} e^{-i\omega_d(t-t_0)} \alpha e^{-i\omega_d t_0} | \mathcal{E} e^{-i\omega_d t_0} \rangle \\
&= \frac{\mathcal{E}}{\sqrt{2\pi}} e^{-i\omega_d t}.
\end{aligned} \tag{B13}$$

where in the third line we used the fact that a coherent state is an eigenstate of the annihilation operator, and that $p_{1,\omega} | \mathcal{E} e^{-i\omega_d t_0} \rangle = 0$ if $\omega \neq \omega_d$.

4. Expression of the reflection coefficient

From $\langle p_1^{\text{in}}(t) \rangle = \mathcal{E}/(\sqrt{2\pi})e^{-i\omega_d t}$, we see that $\langle \tilde{p}_1^{\text{in}}(\omega) \rangle = \mathcal{E}\delta(\omega - \omega_d)$. Thus, assimilating ω to the frequency of the drive, the reflection at port 1 reads

$$\begin{aligned}
r_1(\omega) &= \left. \frac{\tilde{p}_1^{\text{out}}}{\tilde{p}_1^{\text{in}}} \right|_{\tilde{p}_2^{\text{in}}=0} = 1 + \sqrt{\kappa_1} e^{-i\phi_1} \frac{\tilde{c} |_{\tilde{p}_2^{\text{in}}=0}}{\tilde{p}_1^{\text{in}}} \\
&= 1 - i\sqrt{\kappa_1} \frac{\tilde{\Delta}_m \sqrt{\kappa_1}}{A(\omega)} - i\sqrt{\kappa_1} e^{-i\phi_1} \frac{(\tilde{g}' e^{i\phi_3} + \sqrt{\xi} e^{i\phi_3'} \tilde{\Delta}_m) \sqrt{\kappa_3} \tilde{p}_3^{\text{in}}}{A(\omega) \tilde{p}_1^{\text{in}}} \\
&= 1 - i\sqrt{\kappa_1} \frac{\tilde{\Delta}_m \sqrt{\kappa_1} + (\tilde{g}' e^{i(\phi_3 - \phi_1)} + \sqrt{\xi} e^{i(\phi_3' - \phi_1)} \tilde{\Delta}_m) \sqrt{\kappa_3} \delta e^{i\phi}}{A(\omega)}
\end{aligned} \tag{B14}$$

Notice that for $\kappa_3 = 0$ (i.e., only the cavity mode is driven), the expression for the reflection reduces to the S_{11} parameter.

Assuming that port 3 is not active, that is, $\langle p_3^{\text{in}} \rangle = 0$ (which corresponds to $\delta = 0$), the reflection r_1 and transmission t_2 coefficients of Eqs. (B14) and (D1) reduce to

5. Normalization

For a standard coherent state $|\mathcal{E}\rangle$, the mean number of particles is given by $|\mathcal{E}|^2$. Here, the unit of the ports $\langle p_k \rangle$ is $\sqrt{\omega}$, which can be seen by considering the QLEs. Hence, for the ports, $|\mathcal{E}|^2$ is a number of photons per second, which can be linked with the power of the drive P by

$$\mathcal{E} = \sqrt{\frac{P}{\hbar\omega_d}}. \tag{B15}$$

Given that $\langle p_3 \rangle = \delta e^{i\phi} \langle p_1 \rangle$, we deduce that the power difference between port 1 and port 3 is given by δ^2 , which allows us to renormalize the expression of the reflection and transmission.

APPENDIX C: EXPRESSION OF THE REFLECTION AT PORT 1 WITH STANDARD S PARAMETERS

In this appendix, we derive the expressions of the standard S parameters, when only one port is active at a time.

$$S_{11}(\omega) = 1 - i \frac{\tilde{\Delta}_m \kappa_1}{\tilde{\Delta}_c \tilde{\Delta}_m - \tilde{g}\tilde{g}'}, \tag{C1}$$

$$S_{21}(\omega) = -i \frac{\tilde{\Delta}_m \sqrt{\kappa_1 \kappa_2} e^{i(\phi_1 - \phi_2)}}{\tilde{\Delta}_c \tilde{\Delta}_m - \tilde{g}\tilde{g}'}, \tag{C2}$$

which are the standard S parameters for a two-port cavity. Note that by symmetry we also have

$$\begin{aligned}
S_{12}(\omega) &= -i \frac{\tilde{\Delta}_m \sqrt{\kappa_1 \kappa_2} e^{i(\phi_2 - \phi_1)}}{\tilde{\Delta}_c \tilde{\Delta}_m - \tilde{g}\tilde{g}'}, \\
S_{22}(\omega) &= 1 - i \frac{\tilde{\Delta}_m \kappa_2}{\tilde{\Delta}_c \tilde{\Delta}_m - \tilde{g}\tilde{g}'}.
\end{aligned} \tag{C3}$$

Similarly, using Eq. (B7), we find

$$S_{13}(\omega) = \left. \frac{\tilde{p}_1^{\text{out}}}{\tilde{p}_3^{\text{in}}} \right|_{\tilde{p}_1^{\text{in}}=\tilde{p}_2^{\text{in}}=0} = \sqrt{\kappa_1} e^{-i\phi_1} \frac{\tilde{c}_1|_{\tilde{p}_1^{\text{in}}=\tilde{p}_2^{\text{in}}=0}}{\tilde{p}_3^{\text{in}}} = -i\sqrt{\kappa_1\kappa_3} \frac{\tilde{g}' e^{i(\phi_3-\phi_1)} + \sqrt{\zeta} e^{i(\phi_3'-\phi_1)} \tilde{\Delta}_m}{A(\omega)}, \quad (\text{C4})$$

and hence

$$r_1(\omega) = S_{11} + \delta e^{i\phi} S_{13} = 1 - i\sqrt{\kappa_1} \frac{\tilde{\Delta}_m \sqrt{\kappa_1} + \left(\tilde{g}' e^{i(\phi_3-\phi_1)} + \sqrt{\zeta} e^{i(\phi_3'-\phi_1)} \tilde{\Delta}_m \right) \sqrt{\kappa_3} \delta e^{i\phi}}{A(\omega)} \quad (\text{C5})$$

which matches the equation given in the main text for $\zeta = 0$.

APPENDIX D: CALCULATION OF THE TRANSMISSION

Using the results of the input-output theory above, the transmission through port 2 when ports 1 and 3 are active is calculated to be

$$t_2(\omega) = \left. \frac{\tilde{p}_2^{\text{out}}}{\tilde{p}_1^{\text{in}}} \right|_{\tilde{p}_2^{\text{in}}=0} = \sqrt{\kappa_2} e^{-i\phi_2} \frac{\tilde{c}_1|_{\tilde{p}_2^{\text{in}}=0}}{\tilde{p}_1^{\text{in}}} = -i\sqrt{\kappa_2} \frac{\tilde{\Delta}_m \sqrt{\kappa_1} e^{i(\phi_1-\phi_2)} + \left(\tilde{g}' e^{i(\phi_3-\phi_2)} + \sqrt{\zeta} e^{i(\phi_3'-\phi_2)} \tilde{\Delta}_m \right) \sqrt{\kappa_3} \delta e^{i\phi}}{A(\omega)}. \quad (\text{D1})$$

Thus, the normalized transmission at port 2 is $T_2 = 1/(\sqrt{1+\delta^2})t_2$.

1. Expression with S parameters

Furthermore, from Eq. (C4), we see that S_{23} can be obtained from S_{13} by replacing $(\kappa_1, \phi_1) \mapsto (\kappa_2, \phi_2)$, and thus we have

$$S_{23}(\omega) = \left. \frac{\tilde{p}_2^{\text{out}}}{\tilde{p}_3^{\text{in}}} \right|_{\tilde{p}_1^{\text{in}}=\tilde{p}_2^{\text{in}}=0} = \sqrt{\kappa_2} e^{-i\phi_2} \frac{\tilde{c}_1|_{\tilde{p}_1^{\text{in}}=\tilde{p}_2^{\text{in}}=0}}{\tilde{p}_3^{\text{in}}} = -i\sqrt{\kappa_2\kappa_3} \frac{\tilde{g}' e^{i(\phi_3-\phi_2)} + \sqrt{\zeta} e^{i(\phi_3'-\phi_2)} \tilde{\Delta}_m}{A(\omega)}. \quad (\text{D2})$$

Hence, comparing Eq. (D1) with Eqs. (C2) and (D2), we conclude that $t_2 = S_{21} + \delta e^{i\phi} S_{23}$.

2. Zeros of the numerator

The zeros of the numerator of T_2 are given by

$$(\omega - \tilde{\omega}_m) \left[\sqrt{\kappa_1} e^{i(\phi_1-\phi_2)} + \sqrt{\zeta\kappa_3} e^{i(\phi_3'-\phi_2)} \delta e^{i\phi} \right] + \left(g^* - i\sqrt{\zeta} \frac{\kappa_3}{2} e^{i(\phi_3'-\phi_3)} \right) e^{i(\phi_3-\phi_2)} \sqrt{\kappa_3} \delta e^{i\phi} = 0, \quad (\text{D3})$$

that is,

$$\omega = \tilde{\omega}_m + \frac{\left(g^* - i\sqrt{\zeta} \frac{\kappa_3}{2} e^{i(\phi_3'-\phi_3)} \right) e^{i\phi_3} \sqrt{\kappa_3} \delta e^{i\phi}}{\sqrt{\kappa_1} e^{i\phi_1} + \sqrt{\zeta\kappa_3} e^{i\phi_3'} \delta e^{i\phi}}. \quad (\text{D4})$$

APPENDIX E: EXPRESSION FOR THE REFLECTION AT PORT 2 AND THE TRANSMISSION AT PORT 1

In the main text, we only consider that port 1 is being driven, while port 2 is passive and used as a probe. In this note, we exchange the roles of ports 1 and 2 to check that the results are identical. Thus, we now have $\langle p_2^{\text{in}}(t) \rangle = \frac{\varepsilon}{\sqrt{2\pi}} e^{-i\omega_d t}$, $\langle p_3^{\text{in}} \rangle = \delta e^{i\phi} \langle p_1^{\text{in}} \rangle$, and $\langle p_2^{\text{in}} \rangle = 0$. The reflection at port 2 is

$$r_2(\omega) = \left. \frac{\tilde{p}_2^{\text{out}}}{\tilde{p}_2^{\text{in}}} \right|_{\tilde{p}_1^{\text{in}}=0} = 1 + \sqrt{\kappa_2} e^{-i\phi_2} \frac{\tilde{c}_1|_{\tilde{p}_1^{\text{in}}=0}}{\tilde{p}_2^{\text{in}}} = 1 - i\sqrt{\kappa_2} \frac{\tilde{\Delta}_m \sqrt{\kappa_2} + \left(\tilde{g}' e^{i(\phi_3-\phi_2)} + \sqrt{\zeta} e^{i(\phi_3'-\phi_2)} \tilde{\Delta}_m \right) \sqrt{\kappa_3} \delta e^{i\phi}}{A(\omega)}, \quad (\text{E1})$$

and hence it is formally identical to r_1 after replacing the index 1 by 2. For the transmission through port 1,

$$t_1(\omega) = \left. \frac{\tilde{p}_1^{\text{out}}}{\tilde{p}_2^{\text{in}}} \right|_{\tilde{p}_1^{\text{in}}=0} = \sqrt{\kappa_1} e^{-i\phi_1} \frac{\tilde{c}_1|_{\tilde{p}_1^{\text{in}}=0}}{\tilde{p}_2^{\text{in}}} = -i\sqrt{\kappa_1} \frac{\tilde{\Delta}_m \sqrt{\kappa_2} e^{i(\phi_2-\phi_1)} + \left(\tilde{g}' e^{i(\phi_3-\phi_1)} + \sqrt{\zeta} e^{i(\phi_3'-\phi_1)} \tilde{\Delta}_m \right) \sqrt{\kappa_3} \delta e^{i\phi}}{A(\omega)}. \quad (\text{E2})$$

APPENDIX F: EFFECTIVE COUPLING STRENGTH AND CROSSTALK

For nonvanishing coupling of port 3 to the cavity mode, $\zeta \neq 0$, we recall that the reflection coefficient given by Eq. (B14) is

$$\begin{aligned} r_1(\omega) &= \frac{N(\omega)}{D(\omega)} = 1 - i\sqrt{\kappa_1} \frac{\tilde{\Delta}_m \sqrt{\kappa_1} + \left(\tilde{g}' e^{i(\phi_3 - \phi_1)} + \sqrt{\zeta} e^{i(\phi'_3 - \phi_1)} \tilde{\Delta}_m \right) \sqrt{\kappa_3} \delta e^{i\phi}}{A(\omega)} \\ &= \frac{\tilde{\Delta}_c \tilde{\Delta}_m - \tilde{g}\tilde{g}' - i\kappa_1 \tilde{\Delta}_m - \tilde{g}' \sqrt{\kappa_1 \kappa_3} e^{i(\phi_3 - \phi_1)} \delta e^{i\phi} - i\tilde{\Delta}_m \sqrt{\zeta} \sqrt{\kappa_1 \kappa_3} e^{i(\phi'_3 - \phi_1)} \delta e^{i\phi}}{\tilde{\Delta}_c \tilde{\Delta}_m - \tilde{g}\tilde{g}'}. \end{aligned} \quad (\text{F1})$$

The numerator is

$$\begin{aligned} N(\omega) &= \omega^2 - (\tilde{\omega}_c + \tilde{\omega}_m) \omega + \tilde{\omega}_c \tilde{\omega}_m - \tilde{g}\tilde{g}' - i\kappa_1 (\omega - \tilde{\omega}_m) - \tilde{g}' \sqrt{\kappa_1 \kappa_3} \delta e^{i(\phi + \phi_3 - \phi_1)} - i(\omega - \tilde{\omega}_m) \sqrt{\zeta} \sqrt{\kappa_1 \kappa_3} \delta e^{i(\phi + \phi'_3 - \phi_1)} \\ &= \omega^2 - \left(\tilde{\omega}_c + i \left[\kappa_1 + \sqrt{\zeta} \sqrt{\kappa_1 \kappa_3} \delta e^{i(\phi + \phi'_3 - \phi_1)} \right] + \tilde{\omega}_m \right) \omega + \left(\tilde{\omega}_c + i \left[\kappa_1 + \sqrt{\zeta} \sqrt{\kappa_1 \kappa_3} \delta e^{i(\phi + \phi'_3 - \phi_1)} \right] \right) \tilde{\omega}_m \\ &\quad - \tilde{g}\tilde{g}' - \tilde{g}' \sqrt{\kappa_1 \kappa_3} \delta e^{i(\phi + \phi_3 - \phi_1)} \\ &= \omega^2 - (\tilde{\omega}'_c + \tilde{\omega}_m) \omega + \tilde{\omega}'_c \tilde{\omega}_m - \tilde{G}^2, \end{aligned} \quad (\text{F2})$$

where $\omega'_c = \omega_c + i \left[\kappa_1 + \sqrt{\zeta} \sqrt{\kappa_1 \kappa_3} \delta e^{i(\phi + \phi'_3 - \phi_1)} \right]$ and, recalling that $g = |g|e^{i\varphi}$,

$$\begin{aligned} \tilde{G} &= \sqrt{\tilde{g}\tilde{g}' + \tilde{g}' \sqrt{\kappa_1 \kappa_3} \delta e^{i(\phi + \phi_3 - \phi_1)}} \\ &= \sqrt{\left(g - i\sqrt{\zeta} e^{i(\phi_3 - \phi'_3)} \frac{\kappa_3}{2} \right) \left(g^* - i\sqrt{\zeta} e^{-i(\phi_3 - \phi'_3)} \frac{\kappa_3}{2} \right) + i \left(g^* - i\sqrt{\zeta} e^{-i(\phi_3 - \phi'_3)} \frac{\kappa_3}{2} \right) \sqrt{\kappa_1 \kappa_3} \delta e^{i(\phi + \phi_3 - \phi_1)}} \\ &= |g| \sqrt{1 + \frac{\sqrt{\kappa_1 \kappa_3}}{|g|} \delta e^{i(\phi + \phi_3 - \phi_1 + \frac{\pi}{2} - \varphi)} - \frac{\sqrt{\zeta} \kappa_3}{|g|} \left(\frac{\sqrt{\zeta} \kappa_3}{4 |g|} + i \cos(\varphi + \phi'_3 - \phi_3) - \frac{\sqrt{\kappa_1 \kappa_3}}{2 |g|} \delta e^{i(\phi + \phi'_3 - \phi_1)} \right)}. \end{aligned} \quad (\text{F3})$$

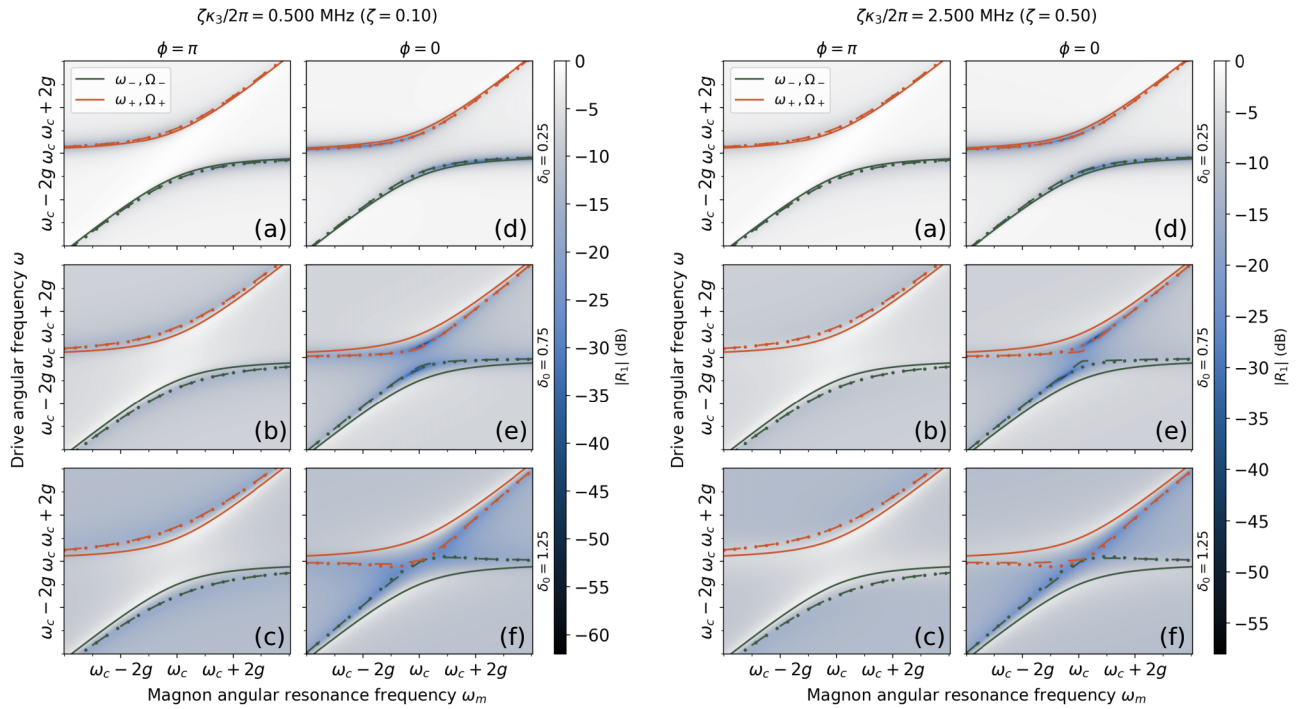


FIG. 5. Plot of the reflection amplitude $|R_1|$ for $\zeta = 0.1$ (left) and $\zeta = 0.5$ (right), with other parameters as in Fig. 2 of the main text. The dashed lines correspond to $\zeta \neq 0$ (they are exactly the same as in Fig. 2 of the main text) while the dots corresponds to $\zeta = 0$.

The first two terms under the square root correspond to the formula given in the main text, which corresponds to $\zeta = 0$. In Fig. 5 we plot the reflection coefficient with parameters identical to those used in the main text, where $\kappa_3/g = 1/2$.

APPENDIX G: SIMPLIFICATION OF THE EFFECTIVE HAMILTONIAN

The effective Hamiltonian in the main text reads

$$H_{\text{eff}} = \hbar\tilde{\omega}_c c^\dagger c + \hbar\tilde{\omega}_m m^\dagger m + \hbar g (cm^\dagger + c^\dagger m) + i\hbar (\mathcal{E}_1 c e^{i\omega t} - \text{h.c.}) + i\hbar (\mathcal{E}_3 m e^{i\omega t} - \text{h.c.}). \quad (\text{G1})$$

To simplify the calculations, we define $\epsilon_c = i\mathcal{E}_1$ and $\epsilon_m = i\mathcal{E}_3$, and we obtain

$$H_{\text{eff}} = \hbar\tilde{\omega}_c c^\dagger c + \hbar\tilde{\omega}_m m^\dagger m + \hbar g (cm^\dagger + c^\dagger m) + \hbar (\epsilon_c c e^{i\omega t} + \epsilon_c^* c^\dagger e^{-i\omega t}) + \hbar (\epsilon_m m e^{i\omega t} + \epsilon_m^* m^\dagger e^{-i\omega t}). \quad (\text{G2})$$

In a frame rotating with the drive, which corresponds to the unitary transformation $U = \exp [i\omega_d t (c^\dagger c + m^\dagger m)]$, we obtain

$$H_{\text{eff}} = \hbar\tilde{\Delta}_c c^\dagger c + \hbar\tilde{\Delta}_m m^\dagger m + \hbar g (cm^\dagger + c^\dagger m) + \hbar (\epsilon_c^* c + \epsilon_c c^\dagger) + \hbar (\epsilon_m^* m + \epsilon_m m^\dagger), \quad (\text{G3})$$

with the detunings $\tilde{\Delta}_c = \tilde{\omega}_c - \omega_d$, $\tilde{\Delta}_m = \tilde{\omega}_m - \omega_d$.

Let us consider the driving terms as a perturbation V , and split the Hamiltonian of Eq. (G3) into $H = H_0 + V$, where

$$H_0 = \hbar\Delta_c c^\dagger c + \Delta_m m^\dagger m + \hbar g (cm^\dagger + c^\dagger m), \quad (\text{G4})$$

$$V = \hbar (\epsilon_c c + \epsilon_c^* c^\dagger) + \hbar (\epsilon_m m + \epsilon_m^* m^\dagger). \quad (\text{G5})$$

We try to find a Schrieffer-Wolff transformation [56] $U = e^\Lambda$ with $\Lambda = (\lambda_c c - \lambda_c^* c^\dagger) + (\lambda_m m - \lambda_m^* m^\dagger)$, and λ_c, λ_m constants such that $V + [\Lambda, H_0] = 0$. Note that $\Lambda^\dagger = -\Lambda$, such that e^Λ is unitary. We have

$$\begin{aligned} V + [\Lambda, H_0] &= \epsilon_c c + \epsilon_c^* c^\dagger + \epsilon_m m + \epsilon_m^* m^\dagger + [\lambda_c c - \lambda_c^* c^\dagger, \hbar\Delta_c c^\dagger c] + [\lambda_c c - \lambda_c^* c^\dagger, \hbar g (cm^\dagger + c^\dagger m)] \\ &\quad + [\lambda_m m - \lambda_m^* m^\dagger, \hbar\Delta_m m^\dagger m] + [\lambda_m m - \lambda_m^* m^\dagger, \hbar g (cm^\dagger + c^\dagger m)] \\ &= \epsilon_c c + \epsilon_c^* c^\dagger + \epsilon_m m + \epsilon_m^* m^\dagger + \hbar\Delta_c (\lambda_c c + \lambda_c^* c^\dagger) + \hbar g (\lambda_c m + \lambda_c^* m^\dagger) \\ &\quad + \hbar\Delta_m (\lambda_m m + \lambda_m^* m^\dagger) + \hbar g (\lambda_m c + \lambda_m^* c^\dagger) \\ &= \hbar [(\epsilon_c + \Delta_c \lambda_c + g\lambda_m) c + (\epsilon_c^* + \Delta_c \lambda_c^* + g\lambda_m^*) c^\dagger] \\ &\quad + \hbar [(\epsilon_m + g\lambda_c + \Delta_m \lambda_m) m + (\epsilon_m^* + g\lambda_c^* + \Delta_m \lambda_m^*) m^\dagger]. \end{aligned} \quad (\text{G6})$$

Imposing $V + [\Lambda, H_0] = 0$ (the Schrieffer-Wolff condition) leads to

$$\begin{cases} \epsilon_c + \Delta_c \lambda_c + g\lambda_m = 0, \\ \epsilon_c^* + \Delta_c \lambda_c^* + g\lambda_m^* = 0, \\ \epsilon_m + g\lambda_c + \Delta_m \lambda_m = 0, \\ \epsilon_m^* + g\lambda_c^* + \Delta_m \lambda_m^* = 0, \end{cases} \quad (\text{G7})$$

where we recognize that we get twice the same constraints by hermiticity. We can reduce the system to

$$\begin{cases} \epsilon_c + \Delta_c \lambda_c + g\lambda_m = 0, \\ \epsilon_m + g\lambda_c + \Delta_m \lambda_m = 0, \end{cases} \quad \begin{cases} g\epsilon_c + g\Delta_c \lambda_c + g^2 \lambda_m = 0, \\ \Delta_c \epsilon_m + g\Delta_c \lambda_c + \Delta_c \Delta_m \lambda_m = 0, \end{cases} \quad (\text{G8})$$

$$\begin{cases} \Delta_c \epsilon_m - g\epsilon_c + (\Delta_c \Delta_m - g^2) \lambda_m = 0, \\ g\lambda_c = -\epsilon_m - \Delta_m \lambda_m, \end{cases} \quad \begin{cases} \lambda_m = \frac{\Delta_c \epsilon_m - g\epsilon_c}{\Delta_c \Delta_m - g^2}, \\ \lambda_c = -\frac{\epsilon_m}{g} - \frac{\Delta_m}{g} \frac{\Delta_c \epsilon_m - g\epsilon_c}{\Delta_c \Delta_m - g^2}. \end{cases} \quad (\text{G9})$$

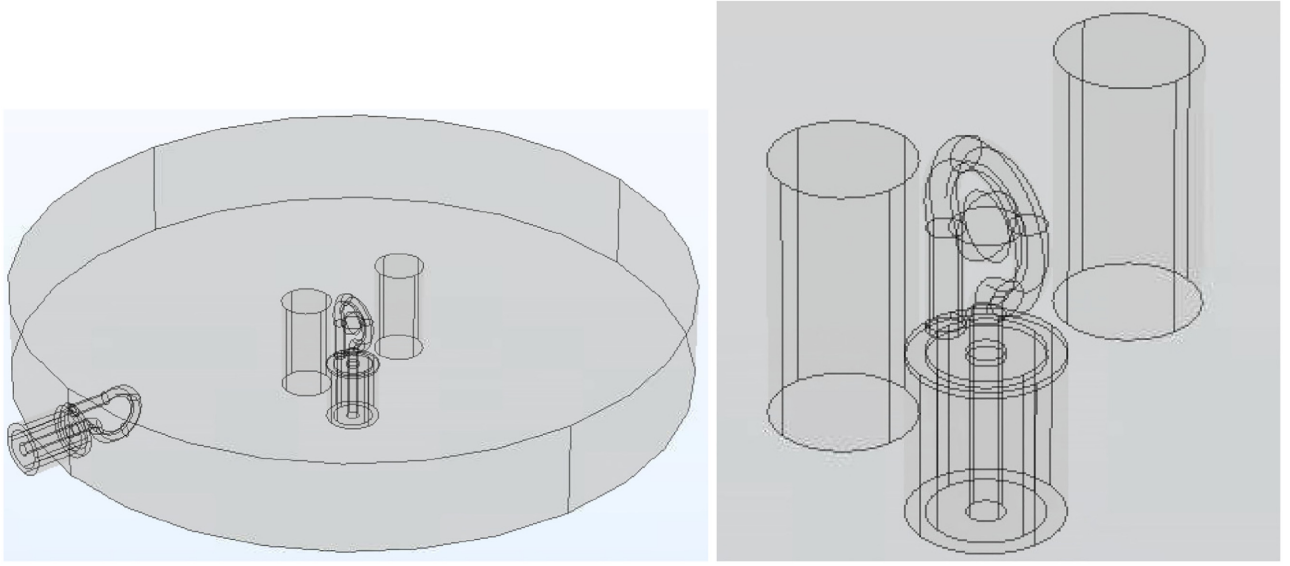


FIG. 6. Model of the two-post cavity we used in the COMSOL MULTIPHYSICS® simulations. The probes for ports 1 and 3 are an exact copy (dimensions and materials) limiting the effects of potential dephasings ϕ_1 and ϕ_3 .

The resulting Hamiltonian is

$$\begin{aligned} H' &= H_0 + \frac{1}{2} [\Lambda, V] + \frac{1}{2} [\Lambda, [\Lambda, V]] + \mathcal{O}(\Lambda^3) \\ &= \hbar \Delta_c c^\dagger c + \hbar \Delta_m m^\dagger m + \hbar g (cm^\dagger + c^\dagger m) \\ &\quad + \frac{1}{2} [\lambda_c c - \lambda_c^* c^\dagger, \hbar (\epsilon_c c + \epsilon_c^* c^\dagger)] \end{aligned}$$

$$\begin{aligned} &+ \frac{1}{2} [\lambda_m m - \lambda_m^* m^\dagger, \hbar (\epsilon_m m + \epsilon_m^* m^\dagger)] \\ &= \hbar \Delta_c c^\dagger c + \hbar \Delta_m m^\dagger m + \hbar g (cm^\dagger + c^\dagger m) \\ &\quad + \frac{\hbar}{2} (\lambda_c \epsilon_c^* + \lambda_c^* \epsilon_c + \lambda_m \epsilon_m^* + \lambda_m^* \epsilon_m). \quad (\text{G10}) \end{aligned}$$

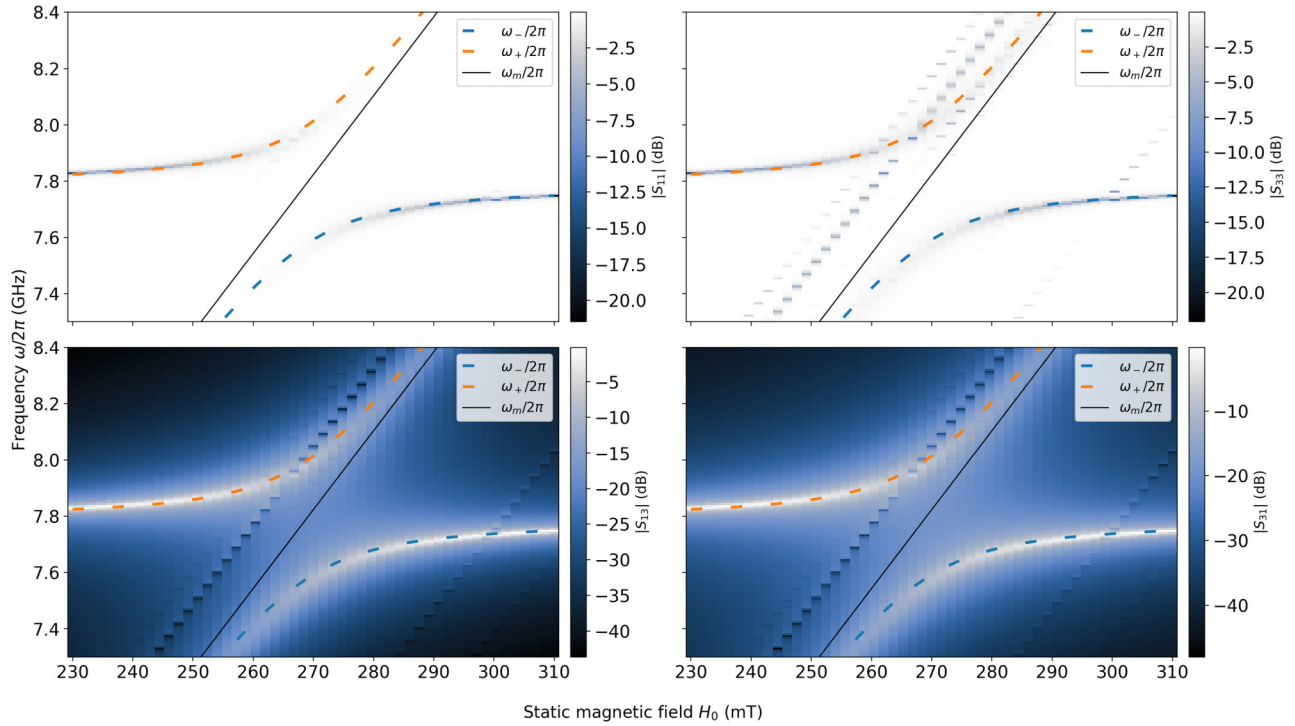


FIG. 7. Numerical calculations of the amplitude of the S parameters of the cavity. The polaritonic frequencies $\omega_{\pm}/2\pi$ are given by Eq. (8) of the main text, and describe level repulsion, the signature of coherent coupling physics. The fit parameters are a coupling strength of $g/2\pi = 210$ MHz and a cavity resonance at $\omega_c/2\pi = 7.853$ GHz.

Note that the transformation is exact, since higher-order commutators vanish (indeed, this is simply a displacement transformation). Furthermore, the last term is simply a constant energy offset with no physical effect, so it can be discarded.

The transformed Hamiltonian H' tells us that under coherent driving of both photons and magnons, the spectrum is equivalent to that of the undriven Hamiltonian H after the substitutions $(\omega_c, \omega_m) \mapsto (\tilde{\omega}_c - \omega_d, \tilde{\omega}_m - \omega_d)$, with $\omega_d/2\pi$ the frequency of the drive. Hence, the standard level repulsion is obtained, and no level attraction can occur.

APPENDIX H: FINITE-ELEMENT MODELING RESULTS

1. Cavity design

In this appendix, we detail the numerical results obtained using the rf module COMSOL MULTIPHYSICS[®] to simulate the two-tone driving experiment described by Fig. 1 in the main text. In the main text, p_1^{in} and p_3^{in} are defined as the signals output by the VNA. Due to differing cable lengths or the geometry of the microwave probes, these signals can be dephased modeled using the phases ϕ_1 and ϕ_3 . To limit these effects as much as possible, we chose to use identical probes for ports 1 and 3. To that end, the probe for port 3 is inserted from the bottom of the cavity instead of on the side, as pictured in Fig. 6.

2. S parameters

We first performed a frequency-domain simulation to obtain the S parameters of the cavity, shown in Fig. 7. As expected, we observe energy level repulsion due to the coherent coupling of the photon and magnon in both reflection and transmission. Therefore, these simulations show that the physics of this system matches that predicted by the Hamiltonian model of Eq. (1) of the main text. We also note the presence of higher-order magnon modes corresponding to diagonal lines offset from the ferromagnetic frequency $\omega_m/2\pi$. This is especially the case for S_{33} , potentially due to the nonuniform magnetic field generated by the loop antenna.

3. Estimation of δ and ϕ_0

Next, we used the numerical values of S_{11} and S_{13} to compute and plot $R_1 = S_{11} + \delta e^{i\phi} S_{13}$ for a range of δ and ϕ . The results, plotted in Fig. 8, allow us very simply to estimate numerically which values of δ and ϕ are required to obtain level repulsion or attraction. We see that level repulsion and attraction are clearly visible for $\delta = 12$ and $\phi \in \{\pi, 0\}$, as predicted by the theory. This implies that the phase offset $\phi_0 = \phi_1 - \phi_3 + \arg g - \pi/2$ in this system is $\phi_0 = \pi$ since level repulsion is obtained when $\phi - \phi_0 = \pi - \phi_0 = 0$. Alternatively, one can extract the linewidths $\kappa_1/2\pi, \kappa_3/2\pi$ and the coherent coupling $|g|/2\pi$ from the S parameters of Fig. 7, and then use $\delta_0 = \sqrt{\kappa_1 \kappa_3} / (|g| \delta)$

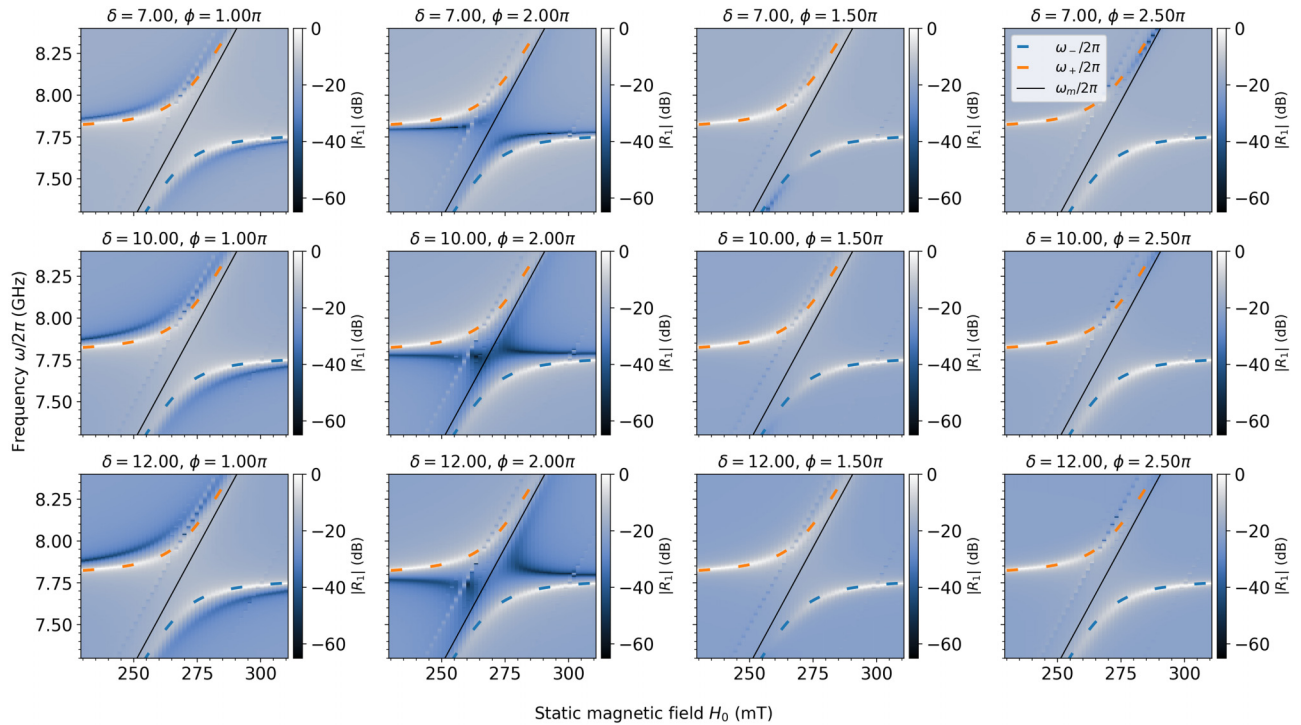


FIG. 8. Numerical calculations of the reflection R_1 using the S parameters obtained using COMSOL MULTIPHYSICS[®]. The legend is common to all figures. The fit parameters are identical to this in Fig. 7.

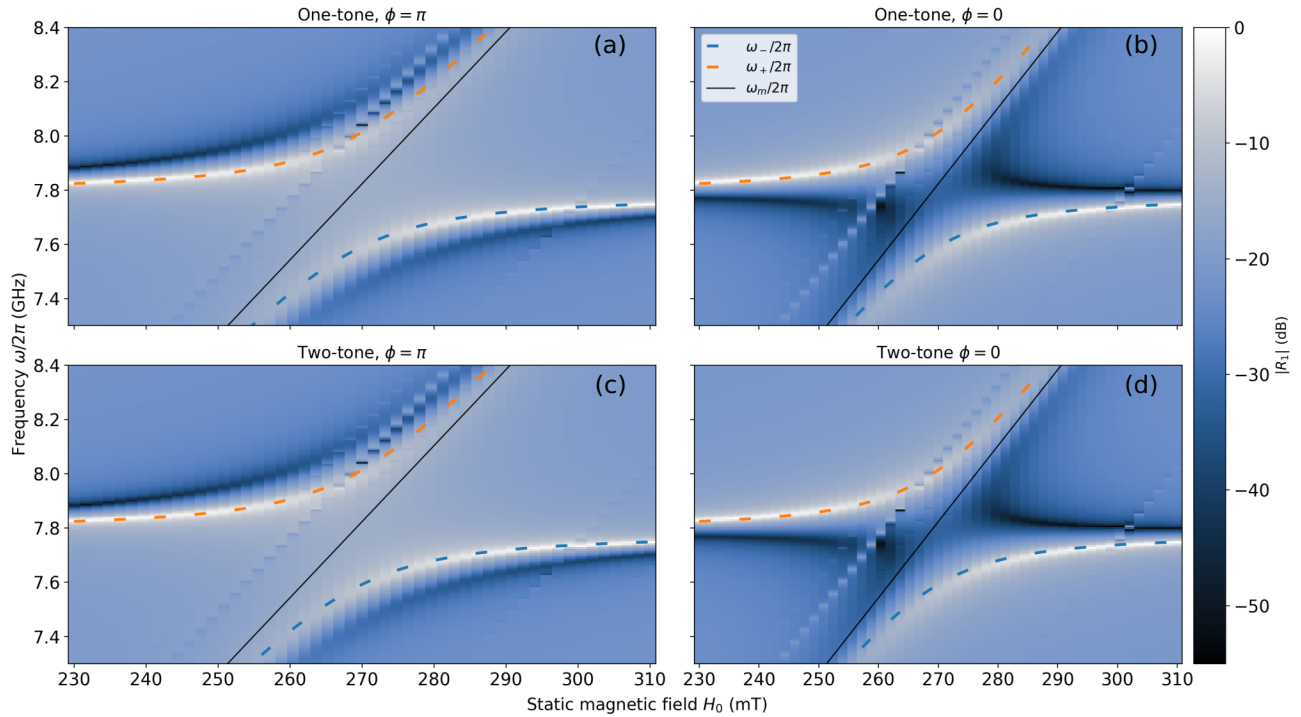


FIG. 9. Numerical calculations of the reflection at port 1 with port 3 active (R_1) using COMSOL MULTIPHYSICS[®] for $\delta = 12$. (a),(b) Evaluation of R_1 from the S parameters using $R_1 = S_{11} + \delta e^{i\phi} S_{13}$. By definition of the S -parameters, these are essentially a combination of one-tone simulations. (c),(d) Fully two-tone simulation where both port 1 and port 3 are simultaneously active.

to estimate δ . Then one needs to sweep the dephasing ϕ between the two drives to determine the phase offset ϕ_0 .

Having determined a suitable δ , we can now perform a true two-tone driving experiment by enabling both port 1 and port 3 in COMSOL MULTIPHYSICS[®]. The results for $\delta = 12$ [Figs. 9(c) and 9(d)] are compared with the manual evaluation of R_1 using the S parameters [Figs. 9(a) and 9(b)]. We observe perfect agreement between the two.

- [1] Lukas Novotny, Strong coupling, energy splitting, and level crossings: A classical perspective, *Am. J. Phys.* **78**, 1199 (2010).
- [2] C. Weisbuch, M. Nishioka, A. Ishikawa, and Y. Arakawa, Observation of the coupled exciton-photon mode splitting in a semiconductor quantum microcavity, *Phys. Rev. Lett.* **69**, 3314 (1992).
- [3] J. M. Dobrindt, I. Wilson-Rae, and T. J. Kippenberg, Parametric normal-mode splitting in cavity optomechanics, *Phys. Rev. Lett.* **101**, 263602 (2008).
- [4] Nicolas Gisin and Rob Thew, Quantum communication, *Nat. Photonics* **1**, 165 (2007).
- [5] H. J. Kimble, The quantum internet, *Nature* **453**, 1023 (2008).
- [6] Dany Lachance-Quirion, Yutaka Tabuchi, Arnaud Glorpe, Koji Usami, and Yasunobu Nakamura, Hybrid quantum systems based on magnonics, *Appl. Phys. Express* **12**, 070101 (2019).

- [7] Chenyang Lu, Bentley Turner, Yongsheng Gui, Jacob Burgess, Jiang Xiao, and Can-Ming Hu, An experimental demonstration of level attraction with coupled pendulums, *Am. J. Phys.* **91**, 585 (2023).
- [8] Yi-Pu Wang and Can-Ming Hu, Dissipative couplings in cavity magnonics, *J. Appl. Phys.* **127**, 130901 (2020).
- [9] M. Harder, B. M. Yao, Y. S. Gui, and C.-M. Hu, Coherent and dissipative cavity magnonics, *J. Appl. Phys.* **129**, 201101 (2021).
- [10] Yi-Pu Wang, J. W. Rao, Y. Yang, Peng-Chao Xu, Y. S. Gui, B. M. Yao, J. Q. You, and C.-M. Hu, Nonreciprocity and unidirectional invisibility in cavity magnonics, *Phys. Rev. Lett.* **123**, 127202 (2019).
- [11] A. Metelmann and A. A. Clerk, Nonreciprocal photon transmission and amplification via reservoir engineering, *Phys. Rev. X* **5**, 021025 (2015).
- [12] Aashish Clerk, Introduction to quantum non-reciprocal interactions: From non-hermitian Hamiltonians to quantum master equations and quantum feedforward schemes, *SciPost Physics Lecture Notes*, 44 (2022).
- [13] Weichao Yu, Jiongjie Wang, H. Y. Yuan, and Jiang Xiao, Prediction of attractive level crossing via a dissipative mode, *Phys. Rev. Lett.* **123**, 227201 (2019).
- [14] Bimu Yao, Tao Yu, Y. S. Gui, J. W. Rao, Y. T. Zhao, W. Lu, and C.-M. Hu, Coherent control of magnon radiative damping with local photon states, *Commun. Phys.* **2**, 1 (2019).
- [15] Bimu Yao, Tao Yu, Xiang Zhang, Wei Lu, Yongsheng Gui, Can-Ming Hu, and Yaroslav M. Blanter, The microscopic

- origin of magnon-photon level attraction by traveling waves: Theory and experiment, *Phys. Rev. B* **100**, 214426 (2019).
- [16] Olivier Bleu, Kenneth Choo, Jesper Levinsen, and Meera M. Parish, Dissipative light-matter coupling and anomalous dispersion in nonideal cavities, *Phys. Rev. A* **109**, 023707 (2024).
- [17] Björn Kubala and Jürgen König, Flux-dependent level attraction in double-dot Aharonov-Bohm interferometers, *Phys. Rev. B* **65**, 245301 (2002).
- [18] W. D. Heiss, The physics of exceptional points, *J. Phys. A: Math. Theor.* **45**, 444016 (2012).
- [19] Dengke Zhang, Xiao-Qing Luo, Yi-Pu Wang, Tie-Fu Li, and J. Q. You, Observation of the exceptional point in cavity magnon-polaritons, *Nat. Commun.* **8**, 1368 (2017).
- [20] Guo-Qiang Zhang and J. Q. You, Higher-order exceptional point in a cavity magnonics system, *Phys. Rev. B* **99**, 054404 (2019).
- [21] Hilary M. Hurst and Benedetta Flebus, Non-hermitian physics in magnetic systems, *J. Appl. Phys.* **132**, 220902 (2022).
- [22] H. Xu, D. Mason, Luyao Jiang, and J. G. E. Harris, Topological energy transfer in an optomechanical system with exceptional points, *Nature* **537**, 80 (2016).
- [23] Yunshan Cao and Peng Yan, Exceptional magnetic sensitivity of Pt-symmetric cavity magnon polaritons, *Phys. Rev. B* **99**, 214415 (2019).
- [24] Tianlin Yu, Huanhuan Yang, Lingling Song, Peng Yan, and Yunshan Cao, Higher-order exceptional points in ferromagnetic trilayers, *Phys. Rev. B* **101**, 144414 (2020).
- [25] Jens Koch, Andrew A. Houck, Karyn Le Hur, and S. M. Girvin, Time-reversal-symmetry breaking in circuit-QED-based photon lattices, *Phys. Rev. A* **82**, 043811 (2010).
- [26] K. M. Sliwa, M. Hatridge, A. Narla, S. Shankar, L. Frunzio, R. J. Schoelkopf, and M. H. Devoret, Reconfigurable Josephson circulator/directional amplifier, *Phys. Rev. X* **5**, 041020 (2015).
- [27] Kejie Fang, Jie Luo, Anja Metelmann, Matthew H. Matheny, Florian Marquardt, Aashish A. Clerk, and Oskar Painter, Generalized non-reciprocity in an optomechanical circuit via synthetic magnetism and reservoir engineering, *Nat. Phys.* **13**, 465 (2017).
- [28] Xinyao Huang, Cuicui Lu, Chao Liang, Honggeng Tao, and Yong-Chun Liu, Loss-induced nonreciprocity, *Light: Sci. Appl.* **10**, 30 (2021).
- [29] Vahram L. Grigoryan, Ka Shen, and Ke Xia, Synchronized spin-photon coupling in a microwave cavity, *Phys. Rev. B* **98**, 024406 (2018).
- [30] Vahram L. Grigoryan and Ke Xia, Cavity-mediated dissipative spin-spin coupling, *Phys. Rev. B* **100**, 014415 (2019).
- [31] Isabella Boventer, Mathias Kläui, Rair Macêdo, and Martin Weides, Steering between level repulsion and attraction: Broad tunability of two-port driven cavity magnon-polaritons, *New J. Phys.* **21**, 125001 (2019).
- [32] Isabella Boventer, Christine Dorflinger, Tim Wolz, Rair Macedo, Romain Lebrun, Mathias Kläui, and Martin Weides, Control of the coupling strength and linewidth of a cavity magnon-polariton, *Phys. Rev. Res.* **2**, 013154 (2020).
- [33] Andreas Barnthaler, Stefan Rotter, Florian Libisch, Joachim Burgdorfer, Stefan Gehler, Ulrich Kuhl, and Hans-Jürgen Stockmann, Probing decoherence through Fano resonances, *Phys. Rev. Lett.* **105**, 056801 (2010).
- [34] Mikhail F. Limonov, Mikhail V. Rybin, Alexander N. Poddubny, and Yuri S. Kivshar, Fano resonances in photonics, *Nat. Photonics* **11**, 543 (2017).
- [35] Qijing Lu, Junqiang Guo, Yan-Lei Zhang, Zixiang Fu, Longxiang Chen, Yifeng Xiang, and Shusen Xie, Level attraction due to dissipative phonon-phonon coupling in an opto-mechano-fluidic resonator, *ACS Photonics* **10**, 699 (2023).
- [36] N. R. Bernier, L. D. Tóth, A. K. Feofanov, and T. J. Kippenberg, Level attraction in a microwave optomechanical circuit, *Phys. Rev. A* **98**, 023841 (2018).
- [37] Nathan R. Bernier, Emanuele G. Dalla Torre, and Eugene Demler, Unstable avoided crossing in coupled spinor condensates, *Phys. Rev. Lett.* **113**, 065303 (2014).
- [38] C. W. Gardiner and M. J. Collett, Input and output in damped quantum systems: Quantum stochastic differential equations and the master equation, *Phys. Rev. A* **31**, 3761 (1985).
- [39] Jeremy Bourhill, Vincent Castel, Alexandre Manchec, and Gwendal Cochet, Universal characterization of cavity-magnon polariton coupling strength verified in modifiable microwave cavity, *J. Appl. Phys.* **128**, 073904 (2020).
- [40] Graeme Flower, Maxim Goryachev, Jeremy Bourhill, and Michael E Tobar, Experimental implementations of cavity-magnon systems: from ultra strong coupling to applications in precision measurement, *New J. Phys.* **21**, 095004 (2019).
- [41] Alan Gardin, Jeremy Bourhill, Vincent Vlaminck, Christian Person, Christophe Fumeaux, Vincent Castel, and Giuseppe C. Tettamanzi, Manifestation of the coupling phase in microwave cavity magnonics, *Phys. Rev. Appl.* **19**, 054069 (2023).
- [42] Guillaume Bourcin, Alan Gardin, Jeremy Bourhill, Vincent Vlaminck, and Vincent Castel, Level attraction in a quasiclosed cavity: Antiresonance in magnonic devices, *Phys. Rev. Appl.* **22**, 064036 (2024).
- [43] Maxim Goryachev, Warrick G. Farr, Daniel L. Creedon, Yaohui Fan, Mikhail Kostylev, and Michael E. Tobar, High-cooperativity cavity qed with magnons at microwave frequencies, *Phys. Rev. Appl.* **2**, 054002 (2014).
- [44] Nikita Kostylev, Maxim Goryachev, and Michael E. Tobar, Superstrong coupling of a microwave cavity to yttrium iron garnet magnons, *Appl. Phys. Lett.* **108**, 062402 (2016).
- [45] J. W. Rao, C. H. Yu, Y. T. Zhao, Y. S. Gui, X. L. Fan, D. S. Xue, and C-M Hu, Level attraction and level repulsion of magnon coupled with a cavity anti-resonance, *New J. Phys.* **21**, 065001 (2019).
- [46] J. W. Rao, P. C. Xu, Y. S. Gui, Y. P. Wang, Y. Yang, Bimu Yao, J. Dietrich, G. E. Bridges, X. L. Fan, D. S. Xue, and C.-M. Hu, Interferometric control of magnon-induced nearly perfect absorption in cavity magnonics, *Nat. Commun.* **12**, 1933 (2021).
- [47] Cristiano Ciuti, Gérald Bastard, and Iacopo Carusotto, Quantum vacuum properties of the intersubband cavity polariton field, *Phys. Rev. B* **72**, 115303 (2005).

- [48] Markus Aspelmeyer, Tobias J. Kippenberg, and Florian Marquardt, Cavity optomechanics, *Rev. Mod. Phys.* **86**, 1391 (2014).
- [49] Klaus Hepp and Elliott H Lieb, On the superradiant phase transition for molecules in a quantized radiation field: The Dicke Maser model, *Ann. Phys. (N. Y)* **76**, 360 (1973).
- [50] T. Holstein and H. Primakoff, Field dependence of the intrinsic domain magnetization of a ferromagnet, *Phys. Rev.* **58**, 1098 (1940).
- [51] Alexandre Le Boité, Theoretical methods for ultrastrong light–matter interactions, *Adv. Quantum Technol.* **3**, 1900140 (2020).
- [52] Fabio Cramerì, Scientific colour maps, (2021).
- [53] Fabio Cramerì, Grace E. Shephard, and Philip J. Heron, The misuse of colour in science communication, *Nat. Commun.* **11**, 5444 (2020).
- [54] Anton Frisk Kockum, Adam Miranowicz, Simone De Liberato, Salvatore Savasta, and Franco Nori, Ultrastrong coupling between light and matter, *Nat. Rev. Phys.* **1**, 19 (2019).
- [55] M. Fox, *Quantum Optics: An Introduction*, Oxford Master Series in Physics (Oxford University Press, Oxford, 2006).
- [56] J. R. Schrieffer and P. A. Wolff, Relation between the Anderson and Kondo Hamiltonians, *Phys. Rev.* **149**, 491 (1966).